# Future Antarctic Climate: Storylines of Midlatitude Jet Strengthening and Shift Emergent from CMIP6

RYAN S. WILLIAMS,[a] GARETH J. MARSHALL,[a] XAVIER LEVINE,[b] LISE S. GRAFF,[c] DÖRTHE HANDORF,[d] NADINE M. JOHNSTON,[a] ALEXEY Y. KARPECHKO,[e] ANDREW ORR,[a] WILLEM JAN VAN DE BERG,[f] RENÉ R. WIJNGAARD,[f] AND PRISCILLA A. MOONEY[b]

[a] *British Antarctic Survey, Cambridge, United Kingdom*
[b] *NORCE Norwegian Research Centre, Bjerknes Centre for Climate Research, Bergen, Norway*
[c] *Norwegian Meteorological Institute, Oslo, Norway*
[d] *Alfred Wegener Institute, Helmholtz Centre for Polar and Marine Research–Research Unit, Potsdam, Germany*
[e] *Finnish Meteorological Institute, Helsinki, Finland*
[f] *Institute for Marine and Atmospheric Research, Utrecht University, Utrecht, Netherlands*

(Manuscript received 3 March 2023, in final form 18 December 2023, accepted 21 December 2023)

ABSTRACT: A main source of regional climate change uncertainty is the large disparity across models in simulating the atmospheric circulation response to global warming. Using the latest suite of global climate models from the sixth phase of the Coupled Model Intercomparison Project (CMIP6), a storyline approach is adopted to derive physically plausible scenarios of Antarctic climate change for 2070–99, according to Shared Socioeconomic Pathway SSP5-8.5. These storylines correspond to differences in the simulated amount of seasonal sea ice loss and either (i) the delay in the summertime stratospheric polar vortex (SPV) breakdown or (ii) wintertime SPV strengthening, which together constitute robust drivers of the response pattern to future climate change. Such changes combined are known to exert a strong control over the Southern Hemisphere midlatitude jet stream, which we quantify as collectively explaining up to 70% of the variance in jet response in summer and 35% in winter. For summer, the expected strengthening and displacement of the tropospheric jet stream varies between a ~1 and 2 m $s^{-1}$ increase and ~2°–4° poleward shift, respectively, across storylines. In both seasons, a larger strengthening of the jet is correlated with less Antarctic warming. By contrast, the response in precipitation is more consistent but still strongly attenuated by large-scale dynamics. We find that an increase in high-latitude precipitation around Antarctica is more pronounced for storylines characterized by a greater poleward jet shift, particularly in summer. Our results highlight the usefulness of the storyline approach in illustrating model uncertainty and understanding the processes that determine the spread in projected Antarctic regional climate response.

SIGNIFICANCE STATEMENT: Uncertainty in future climate predictions for the Antarctic is dominated by the unknown response of the large-scale (global) atmospheric circulation. In characterizing such uncertainty, plausible outcomes of climate response (storylines) are generated from the organization of model projections according to the amount of simulated seasonal sea ice loss and the delay in summertime breakdown/winter strengthening of the stratospheric westerly circulation (polar vortex). The intensity and location of the tropospheric jet stream is strongly dependent on both factors, which strongly influences the near-surface climate response over Antarctica. We find that the simulated amount that Antarctic air temperatures increase by in the future (to the end of the century) is intrinsically related to the projected intensification of the Southern Hemisphere tropospheric jet, varying by a factor of 2 or more across storylines for summer. Storylines with greater jet strengthening are associated with less Antarctic warming (reduced poleward advection of air masses from lower latitudes). Similar differences are found for changes in jet position, which we note has a much stronger control on mid- to high-latitude precipitation response. This includes both an enhanced wetting response around Antarctica and drying response farther equatorward, for storylines characterized by a greater poleward jet shift.

KEYWORDS: Antarctica; Sea ice; Jets; Stratosphere; Climate change; Regression analysis

## 1. Introduction

Climate projections are traditionally summarized by averaging over a large multimodel suite (the ensemble approach), such as produced for Intergovernmental Panel on Climate Change (IPCC) assessments. This approach, however, neglects the wide spread across multimodel suites and fails to utilize important information that can reduce uncertainty (Palmer et al. 2005; Tebaldi and Knutti 2007). Global climate model (GCM) projections of regional climate change are often inconsistent due to the dominant role of internal (regional) atmospheric variability in the extratropics (Deser et al. 2012), to

Denotes content that is immediately available upon publication as open access.

Supplemental information related to this paper is available at the Journals Online website: https://doi.org/10.1175/JCLI-D-23-0122.s1.

*Corresponding author*: Ryan S. Williams, rywill@bas.ac.uk

DOI: 10.1175/JCLI-D-23-0122.1

which the response of the atmospheric circulation is largely unknown (Shepherd 2014). At high latitudes, the disparity in climate projections is, furthermore, particularly acute owing to the physical manifestation of "polar amplification," principally related to both snow and ice albedo and other radiative feedbacks (Schneider et al. 2010; Pithan and Mauritsen 2014; Goosse et al. 2018), which further amplifies the uncertainty in atmospheric circulation response. The role of internal variability within the climate system in influencing future climate projections, as the leading source of uncertainty across multimodel ensembles, can therefore be well approximated by sampling the intermodel spread in atmospheric circulation response.

In the Southern Hemisphere extratropics, models are consistent in projecting a poleward shift and intensification of the midlatitude jet stream (Yin 2005; Bracegirdle et al. 2018; Deng et al. 2022) and a reduction in Antarctic sea ice throughout the year (England et al. 2018; Roach et al. 2020), in response to anthropogenic climate change during the twenty-first century. Large intermodel spread in the magnitude of these changes, however, highlights the high uncertainty across multimodel ensemble suites, of which the atmospheric circulation response is likely a significant contributing factor (Shepherd 2014; Screen et al. 2018). In the absence of any foreseeable cross-model consensus concerning this aspect, novel and more sophisticated approaches to exploring climate uncertainty in GCMs have been developed in recent years. For instance, percentile-based methods have been used to sample intermodel spread for Coupled Model Intercomparison Project (CMIP) projections (e.g., Cos et al. 2022; John et al. 2022). Machine learning techniques (e.g., *k*-means clustering) have also been applied to assess the ability of models to represent historical atmospheric circulation regimes (e.g., Cannon 2020; Chen et al. 2022; Dorrington et al. 2022), under the premise that models which perform better in the recent past are more likely to yield realistic future projections. Another method involves identifying a few select, robust features of climate change and characterizing the patterns of climate response for different variables of interest according to the magnitude of change in each feature. This is the concept of the climate storyline approach in which features that are distantly related (remote drivers) are selected on the basis of known physical connections to the wider climate response and used as predictors within a multiple linear regression (MLR) framework (Zappa and Shepherd 2017). The storyline approach therefore has the benefit of enabling a greater understanding of the dynamic or thermodynamic drivers of regional climate change, which alternative approaches fail to provide.

A key driver of Antarctic climate change is the location and strength of the eddy-driven midlatitude jet stream, hereafter jet, which is intrinsically related to the leading mode of variability in the Southern Hemisphere (SH) extratropical zonal circulation, the Southern Annular Mode (SAM) (Rogers and van Loon 1982; Limpasuvan and Hartmann 1999; Thompson and Wallace 2000). Note however that usage of the SAM index as a proxy for mean-state jet response on centennial time scales can be problematic, as such changes are typically much larger in amplitude than transient anomalies in the strength of the westerlies best represented by such index (Swart et al. 2015; Bracegirdle et al. 2018). Understanding how the jet may respond to known remote drivers is imperative as it, and its associated midlatitude storm tracks, strongly modulates the meridional transport of heat and moisture toward Antarctica (Chemke et al. 2022); in turn directly impacting the climate of Antarctica (Thompson and Solomon 2002). Additionally, the near-uniform distribution of land and ocean around Antarctica promotes strong coupling between atmosphere and ocean via changes in surface wind stress. This has implications for Southern Ocean carbon uptake (Lenton and Matear 2007; Hauck et al. 2013; Landschützer et al. 2016), mixed-layer depth, and subsurface warming (Meredith and Hogg 2006; Screen et al. 2010; Sallée et al. 2010), as well as the behavior and properties of the Antarctic Circumpolar Current (Gille 2008; Allison et al. 2010; Spence et al. 2014).

A poleward shift and intensification of the SH midlatitude jet has been observed in recent decades, which can be partially attributed to the springtime SH ozone hole, with the largest jet shift and intensification in the troposphere occurring in austral summer (e.g., Thompson and Solomon 2002; Son et al. 2008, 2009; Polvani et al. 2011). It is also recognized that internal variability has contributed significantly to this trend. For instance, Purich et al. (2016) demonstrated that CMIP5 models forced by ozone depletion underestimate the observed strengthening of the jet, with evidence for a strong seasonal and longitudinal dependency of teleconnection influences, emanating particularly from the tropical Pacific, upon both jet strengthening and shift (e.g., Schneider et al. 2015; Waugh et al. 2020). Yang et al. (2020) also presented evidence for the additional role of internal tropical Pacific sea surface temperature (SST) variability, operating mainly on interdecadal time scales, in contributing to the poleward SH jet shift in recent decades.

A subsequent delay in the seasonal breakdown of the stratospheric polar vortex (SPV), in response to ozone depletion-led stratospheric cooling (enhanced meridional temperature gradient), manifests as a positive SAM tendency that propagates down into the troposphere on typical time scales of 1–2 months (Sun et al. 2014). As the ozone hole is expected to recover during the twenty-first century (Eyring et al. 2013), a partial to nearly full offset of this trend can be anticipated in coming decades, dependent on the greenhouse gas (GHG) emission scenario (Polvani et al. 2011). A return to 1980s levels is estimated around 2066 (between 2049 and 2077) according to the latest Scientific Assessment of Ozone Depletion Report (WMO 2022), assuming full compliance with the Montreal Protocol under Shared Socioeconomic Pathway SSP2-4.5, with indication of a slightly earlier recovery according to some earlier studies under higher representative concentration pathway (RCP)-driven emission scenarios (Dhomse et al. 2018; Amos et al. 2020).

The twenty-first-century evolution of the midlatitude jet location and strength is thus expected to be impacted strongly by the GHG forcing pathway, which also promotes a cooling tendency and strengthened pole-to-equator temperature gradient in the lower stratosphere (Ceppi and Shepherd 2019), together with the rate of ozone recovery in summer especially (Thompson et al. 2011; Orr et al. 2012; Bracegirdle et al. 2020). In particular, Mindlin et al. (2021) demonstrates a tug-of-war between ozone recovery and the GHG effect in terms

of the response of the summertime stratosphere through the twenty-first century, according to CMIP6 models, with direct implications on tropospheric circulation. GCMs are consistent in projecting that the SH midlatitude jet will both strengthen and shift poleward under multiple GHG emission scenarios or SSPs, at least relative to a mid-twentieth century or earlier baseline (IPCC 2022). The tropospheric jet thus acts as an important mediator in influencing the climate response of the Southern Ocean and Antarctic continent. While such a feature is closely related to the strength of the SPV, it is important to recognize that the SPV is more directly related to other influences, as demonstrated in Mindlin et al. (2020, hereafter M20). They examined the combined influence of projected wintertime SPV strengthening/delayed summer breakdown, in conjunction with upper-tropospheric tropical warming (TW), as two remote driver influences that impact large-scale tropospheric circulation via modulation to the latitudinal temperature gradient in the upper troposphere and lower stratosphere.

A third remote driver that was not considered in M20 is that of the projected loss in overall climatological-mean sea ice extent (SIE) by the end of the century, which is robustly simulated by virtually all CMIP6 models in response to future warming, at least according to SSP5-8.5 (Roach et al. 2020). It is important to note that sea ice decline has an opposing effect on the strength and perhaps to a lesser extent the latitude of the SH jet relative to SPV strengthening/delayed breakdown (Bader et al. 2013; England et al. 2018; Bracegirdle et al. 2018). While the latter increases the upper-tropospheric meridional temperature gradient and shifts the jet poleward, sea ice loss decreases the lower-tropospheric latitudinal gradient, forcing a weakening and equatorward shift. This is shown, for example, by Smith et al. (2022) for the Northern Hemisphere and supported in GCM projections for the SH (e.g., Bracegirdle et al. 2018). The sensitivity of the midlatitude jet to each driver may differ in terms of latitude and strength. An overall consensus is however lacking due to the tug-of-war between tropical and polar forcing, the latter including both SPV strengthening and sea ice loss (Chen et al. 2020). It is worth recognizing that Antarctic SIE is responsive to circulation anomalies, such as associated with El Niño–Southern Oscillation and as captured by the SAM index (dependent upon season and time scale), which serves only to complicate the role of sea ice on perturbing the midlatitude jet (Simpkins et al. 2012; Kohyama and Hartmann 2016; Doddridge and Marshall 2017).

The SH midlatitude jet is therefore an ideal candidate for the storyline approach. In this study, we adopt a storyline approach that utilizes a predictor pairing that includes sea ice decline and delay in the SPV breakdown (summer), in addition to sea ice decline and SPV strengthening (winter), as remote tropospheric and stratospheric drivers (i.e., representing the impacts of GHG increases, stratospheric ozone recovery, and sea ice loss). The goals of this study are to 1) provide a unique set of end-of-century (2070–99) storylines of plausible regional climate change scenarios, using a different predictor pairing more tailored to high latitudes compared to M20, and 2) identify global projections best representative of each storyline from CMIP6, for applications such as dynamical downscaling using regional climate models (RCMs), to further explore the regional climate response at much finer resolution. As a prior step, we investigate the performance of the CMIP6 historical simulations and exclude models identified as outliers which may potentially confound the results. The remainder of this paper is structured as follows: data and methods used are described in section 2, with the storyline results subsequently presented for both summer and winter respectively in sections 3 and 4. Finally, the results are discussed in section 5 and conclusions outlined in section 6.

## 2. Data and methods

### a. Data

In constructing our storylines, we utilized output from the full suite of available CMIP6 models with monthly-mean sea ice concentration, zonal wind at 50 hPa (U50), and 2-m air temperature (T2m) fields, accessible using cloud infrastructure (see the data availability statement at the end of the article), listed in Table 1. We used data from the CMIP6 historical simulations extending back to at least 1940 (Eyring et al. 2016) and the ScenarioMIP experiments extending out to at least 2100 (O'Neill et al. 2016); the latter including those corresponding to an 8.5 W $m^{-2}$ increase in radiative forcing by 2100 (SSP5-8.5). A comprehensive overview is provided in Table 1. We considered only the first available model realization (typically r1i1p1f1) in our analyses, as the sensitivity of the results to internal model variability, assessed by comparing different ensemble members, was found to be small for a subset of models investigated (Fig. S1 in the online supplemental material).

In calculating all changes, the climatological mean difference is computed between a future (2070–99) and historical baseline predating the ozone hole (1940–69), as the focus of this study is to explore model projection dependencies primarily driven by the GHG effect. Both an extended austral summer [December–March (DJFM)] and winter [June–August (JJA)] season were selected for our storyline analysis. This is consistent with the seasons examined in M20, except that we included an extra month for summer to ensure the timing of the sea ice seasonal minimum is fully represented (typically in late February). To evaluate model fidelity during the historical period, we extracted monthly mean sea ice concentration, zonal wind, and T2m fields from the fifth generation of the European Centre for Medium-Range Weather Forecasts (ECMWF) reanalysis (ERA5; Hersbach et al. 2020). A later historical baseline (1985–2014), hereafter reference period, was chosen for this comparison as the observational density, and thus quality of the reanalysis, is higher in the satellite era (post-1980). The assimilation of satellite sounder measurements especially has been shown to have markedly improved reanalysis accuracy at SH high latitudes (e.g., Marshall et al. 2022).

### b. Definition of storyline drivers

The two remote drivers (predictors) that we selected, SIE loss and wintertime SPV strengthening/delay in summer SPV

TABLE 1. List of CMIP6 models and realizations used. The horizontal resolution (latitude–longitude output grid dimensions and nominal resolution) for the atmosphere is provided. All details were extracted from https://wcrp-cmip.github.io/CMIP6_CVs/.

| Institution | Model | Realization | Horizontal resolution |
|---|---|---|---|
| BCC | BCC-CSM2-MR | r1i1p1f1 | 160 × 320; 100 km |
| CAMS | CAMS-CSM1-0 | r1i1p1f1 | 160 × 320; 100 km |
| CAS | FOALS-f3-L | r1i1p1f1 | 180 × 360; 100 km |
| | FGOALS-g3 | r1i1p1f1 | 80 × 180; 250 km |
| | CAS-ESM2-0 | r1i1p1f1 | 128 × 256; 100 km |
| CCCma | CanESM5 | r1i1p1f1 | 64 × 128; 500 km |
| | CanESM5-CanOE | r1i1p1f2 | 64 × 128; 500 km |
| CMCC | CMCC-CM2-SR5 | r1i1p1f1 | 192 × 288; 100 km |
| | CMCC-ESM2 | r1i1p1f1 | 192 × 288; 100 km |
| CNRM-CERFACS | CNRM-CM6-1 | r1i1p1f2 | 128 × 256; 250 km |
| | CNRM-CM6-1-HR | r1i1p1f2 | 360 × 720; 100 km |
| | CNRM-ESM2-1 | r1i1p1f2 | 128 × 256; 250 km |
| CSIRO | ACCESS-ESM1-5 | r1i1p1f1 | 145 × 192; 250 km |
| CSIRO-ARCCSS | ACCESS-CM2 | r1i1p1f1 | 144 × 192; 250 km |
| E3SM-Project | E3SM-1-1 | r1i1p1f1 | 180 × 360; 100 km |
| EC-Earth-Consortium | EC-Earth3 | r1i1p1f1 | 256 × 512; 100 km |
| | EC-Earth3-CC | r1i1p1f1 | 256 × 512; 100 km |
| | EC-Earth-Veg | r1i1p1f1 | 256 × 512; 100 km |
| | EC-Earth-Veg-LR | r1i1p1f1 | 160 × 320; 250 km |
| FIO-QLNM | FIO-ESM-2-0 | r1i1p1f1 | 192 × 288; 100 km |
| INM | INM-CM4-8 | r1i1p1f1 | 120 × 180; 100 km |
| | INM-CM5-0 | r1i1p1f1 | 120 × 180; 100 km |
| IPSL | IPSL-CM6A-LR | r1i1p1f1 | 143 × 144; 250 km |
| KIOST | KIOST-ESM | r1i1p1f1 | 96 × 192; 250 km |
| MIROC | MIROC-ES2L | r1i1p1f2 | 64 × 128; 500 km |
| | MIROC6 | r1i1p1f1 | 128 × 256; 250 km |
| MOHC | HadGEM3-GC31-LL | r1i1p1f3 | 144 × 192; 250 km |
| | HadGEM3-GC31-MM | r1i1p1f3 | 324 × 432; 100 km |
| | UKESM1-0-LL | r1i1p1f2 | 144 × 192; 250 km |
| MPI-M | MPI-ESM1-2-LR | r1i1p1f1 | 96 × 192; 250 km |
| | MPI-ESM1-2-HR | r1i1p1f1 | 192 × 384; 100 km |
| MRI | MRI-ESM2-0 | r1i1p1f1 | 160 × 320; 100 km |
| NASA-GISS | GISS-E2-1-G | r1i1p3f1 | 90 × 144; 250 km |
| NOAA-GFDL | GFDL-CM4 | r1i1p1f1 | 180 × 360; 100 km |
| | GFDL-ESM4 | r1i1p1f1 | 180 × 360; 100 km |
| NCAR | CESM2 | r4i1p1f1 | 192 × 288; 100 km |
| | CESM2-WACCM | r1i1p1f1 | 192 × 288; 100 km |
| NCC | NorESM2-LM | r1i1p1f1 | 96 × 144; 250 km |
| | NorESM2-MM | r1i1p1f1 | 192 × 288; 100 km |
| NUIST | NESM3 | r1i1p1f1 | 96 × 192; 250 km |
| THU | CIESM | r1i1p1f1 | 192 × 288; 100 km |

breakdown, were found to be statistically uncorrelated with each other across all models, which is an important condition that needs to be satisfied in the storyline framework. We derived representative values for each model, scaled per °C of global warming, by normalizing against the global-mean annual mean temperature change between the historical and future periods. This effectively removes any influence of differences in climate response between the models we examined, serving to elucidate more clearly variations in the pattern of the climate response for a given target variable (Zappa and Shepherd 2017; M20).

We calculated model values of SIE as the hemispheric sum of the area of the grid cells for which the sea ice concentration is at least 15% (the standard threshold between ice and open water). SIE loss was then computed as the difference between the future and historical values for each respective season. We quantified the change in the strength of the SPV as the difference in the seasonal-mean U50 between historical and future, area-averaged for the latitude range 50°–60°S, consistent with that used in M20 for winter. For summer, the change in U50 averaged for November–December ($U50_{ND}$) was used as a proxy for the SPV breakdown, to correspond broadly with the timing of this event and account for the established one-to-two-month delay on tropospheric circulation impact (e.g., Sun et al. 2014). In our case, the sensitivity of different target variables to the delay in SPV breakdown (e.g., spatial fields in 850-hPa zonal wind; U850) were found to be significantly weaker compared to the mean change in $U50_{ND}$. However, we found the correlation between the vortex breakdown delay and the change in $U50_{ND}$ to be high ($r > 0.7$), for the

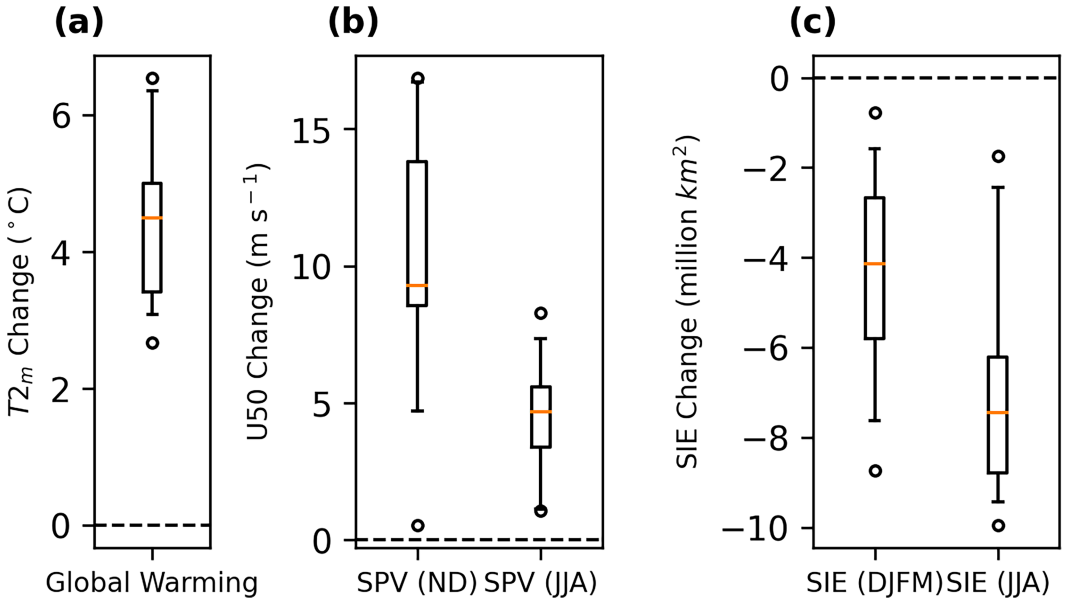


FIG. 1. Box-and-whisker plot of the CMIP6 model spread (after excluding outliers) in (a) projected global warming (annual-mean, global mean T2m change), (b) U50 change, and (c) SIE loss calculated for both summer and winter according to SSP5-8.5, computed as the end-of-the-century (2070–99) minus the selected pre-ozone hole historical baseline (1940–69) difference. The orange line denotes the median, and the box represents the interquartile range, with whiskers extending to the 95% confidence limits. Models outside this range are denoted by individual circles.

subset of models with daily zonal wind fields, ensuring confidence that this term could be used as a reliable proxy. An advantage of switching this term is that a larger number of realizations (models) could be included since monthly U50 fields are more numerous than daily fields within the CMIP6 archive. For simplicity, we therefore refer to this predictor hereafter as SPV strengthening for both seasons, as each term constitutes the change in 50-hPa wind strength between future and historical periods, except again later in section 5 (discussion) and section 6 (conclusions).

The median, interquartile range, 95% confidence limits and any models outside this range are shown in Fig. 1 for the distribution in model global warming, together with the seasonal change in U50 and SIE for both seasons, after excluding those identified as outliers (see the historical assessment section in the supplemental material). Any model calculated to be outside two standard deviations ($2\sigma$) either side of the multimodel mean for at least one month in each season (summer and winter), for either U50 (Fig. S2) or SIE (Fig. S3a), was not considered in generating the storylines developed here. For SIE, models were also omitted if the computed integrated ice edge error (IIEE), a metric quantifying both the cumulative error in sea ice edge placement and absolute error in SIE relative to a reference observational dataset (Goessling et al. 2016), exceeded 80% of the total amount of SIE for any given month, with respect to ERA5 (Fig. S3b). In Fig. 1a, all models are included apart from four models (MIROC-ES2L, MIROC6, FGOALS-g3, and FGOALS-f3-L) that were omitted for both seasons ($n = 37$ from an initial suite of 41 available models). For each individual season examined and displayed in Figs. 1b and 1c, a total of nine models are omitted for summer ($n = 32$) and six models omitted for winter ($n = 35$). We confirm that the observed (ERA5) relationship between the seasonal-mean jet strength/position and both SH SIE and SPV strength (U50) interannually for the last 30 years of the historical simulations is well within the range of all models included (Figs. S4 and S5).

Although we do not include upper-tropospheric TW as a predictor in generating our storylines here, which usefully simplifies interpretation of the results by considering only two remote drivers, we did assess the role of such influence on jet response, for which we use U850 as a proxy, in supporting our findings (Fig. S6). As in M20, we evaluated the influence of this additional remote driver by computing the zonally averaged change in temperature at 250 hPa between 15°S and 15°N between the future (2070–99) and historical (1940–69) period. We also place our results in the context of the findings from M20 to ascertain the role of each influence on the climatological jet strength and location, since the SPV predictor used here is essentially equivalent. The storyline approach adopted here has been optimized to explain as much variance in the change in the midlatitude jet as possible, using just two remote drivers (predictors), particularly relevant to Antarctic climate.

### c. *Storyline framework robustness*

#### 1) MLR REGRESSION

The MLR equations, formulated using the framework by Zappa and Shepherd (2017), for each season [Eq. (1): summer and Eq. (2): winter] are

$$P_{xm} = a_x + b_x\left(\frac{\Delta \mathrm{SIE}_{\mathrm{DJFM}}}{\Delta T}\right)'_m + c_x\left(\frac{\Delta \mathrm{U50}_{\mathrm{ND}}}{\Delta T}\right)'_m + d_{xm}, \quad (1)$$

$$P_{xm} = a_x + b_x\left(\frac{\Delta \mathrm{SIE}_{\mathrm{JJA}}}{\Delta T}\right)'_m + c_x\left(\frac{\Delta \mathrm{U50}_{\mathrm{JJA}}}{\Delta \mathrm{T}}\right)'_m + d_{xm}, \quad (2)$$

where $P_{xm}$ represents the pattern of climate response of a given target variable (e.g., U850 or precipitation), in which notation $x$ refers to each grid point (latitude, longitude) and $m$ models. The term $a_x$ represents the global-warming scaled multimodel mean response of that target parameter (for use as the dependent variable to be regressed onto each predictor combined); $b_x$ the regression coefficient calculated from the standardized anomaly in the SIE change (loss) predictor (scaled by global warming) for each model, with respect to the multimodel mean scaled response; $c_x$ the regression coefficient equivalently derived from the change in U50 predictor. The term $\Delta T$ represents the future minus historical difference in annual-mean global-mean temperature (i.e., global warming) used in normalizing each predictor term. Note that while the regression coefficients ($b_x$ and $c_x$) vary spatially, the values in parentheses only vary across models. Collectively, all terms therefore vary both spatially (between grid points) and between models. The term $d_{xm}$ constitutes all other influences on $P_{xm}$ not captured by the MLR model.

Note that in computing the multimodel mean response for each target variable ($a_x$), all fields were first bilinearly interpolated to a common grid, equivalent to a spectrally truncated T42 (~2.8°) horizontal resolution, which corresponds approximately to the grid of the coarsest-resolution model (see Table 1). In computing term $a_x$, the pattern of response is necessarily scaled by the amount of global warming simulated by each model first, to ensure that the uncertainty in global warming level is isolated from the uncertainty in pattern response (Zappa and Shepherd 2017; M20), in which this storyline approach seeks to examine.

### 2) Predictor influence on U850

In diagnosing the skill of the two seasonal MLR models in capturing changes in the SH midlatitude jet, a map of the seas surrounding Antarctica (Fig. 2) is included to help relate the spatial patterns in the sensitivity of U850 to each regression term and the total explained variance geographically. Figure 3 shows the sensitivity of U850 to each of the two predictor terms for each season, together with the total explained variance provided from using both terms. Here, the U850 response is a good indicator of midlatitude jet response which are both equivalent barotropic in nature (Thompson and Wallace 2000).

For summer, U850 appears to be more sensitive to a 1$\sigma$ change in $\mathrm{U50}_{\mathrm{ND}}$ than SIE (computed over DJFM) and is evidently more sensitive overall, by approximately a factor of 2 (offshore of East Antarctica) or more, to SPV strengthening compared to SIE loss computed over the respective period (Figs. 3a,b). The physical robustness of this finding cannot, however, be inferred here due to the large spread in simulated SIE in both the historical and future period (Fig. S3a). As evidenced in Fig. 3a, the response in U850 is nonetheless sensitive to the SIE predictor over the Amundsen–Bellingshausen

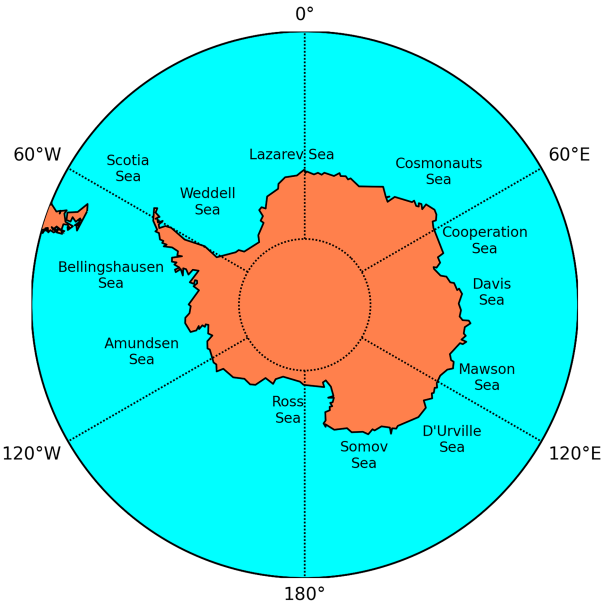


FIG. 2. Map of sea names surrounding the Antarctic continent in the Southern Ocean.

Sea and from the Cooperation Sea eastward to the Somov Sea. A statistically significant signal from U50 (Fig. 3b) is evident across all longitudes, with a dipole pattern apparent between ~55°–70°S and ~35°–45°S. The closer intermodel agreement in climatological monthly-mean U50 is confirmed from Fig. S2, which is consistent with this finding. The geographical pattern of sensitivity to each predictor is largely consistent, such that the signal is mostly self-reinforcing with weaker SIE loss and larger increase in U50 (positive sensitivity) resulting in greater strengthening of the tropospheric jet. With reference to the overlaid historical 8 m $s^{-1}$ U850 contour, indicating the approximate position of the climatological-mean jet, the sensitivity to each predictor is maximized with a poleward offset relative to the latitude of strongest zonal flow, highlighting the clear and pronounced poleward shift in association with less SIE decline and SPV strengthening according to the suite of CMIP6 models used. The explained variance field shows a bimodal structure, with an $r^2$ value of up to 0.7 (70% explained variance) where the sensitivity is largest, with a lack of explained variance in between the jet affected region and the corresponding subtropical high pressure belt at lower latitudes, which is very similar to Fig. 5c in M20 despite their alternative combination of storyline predictors. Comparing these results with the addition of a third upper tropospheric TW predictor (Fig. S6a), U850 is most sensitive in DJFM at lower latitudes to that shown for the $\mathrm{U50}_{\mathrm{ND}}$ predictor (further reinforcing the strengthening and perhaps poleward shift of the jet in models with greater TW). The explained variance of the MLR model increases by definition (Fig. S6b), but with the largest increase also at lower latitudes, confirming that this predictor is less relevant to understanding Antarctic climate response.

In winter, the geographical pattern of the sensitivity in U850 to each of the SIE loss and U50 predictors is qualitatively

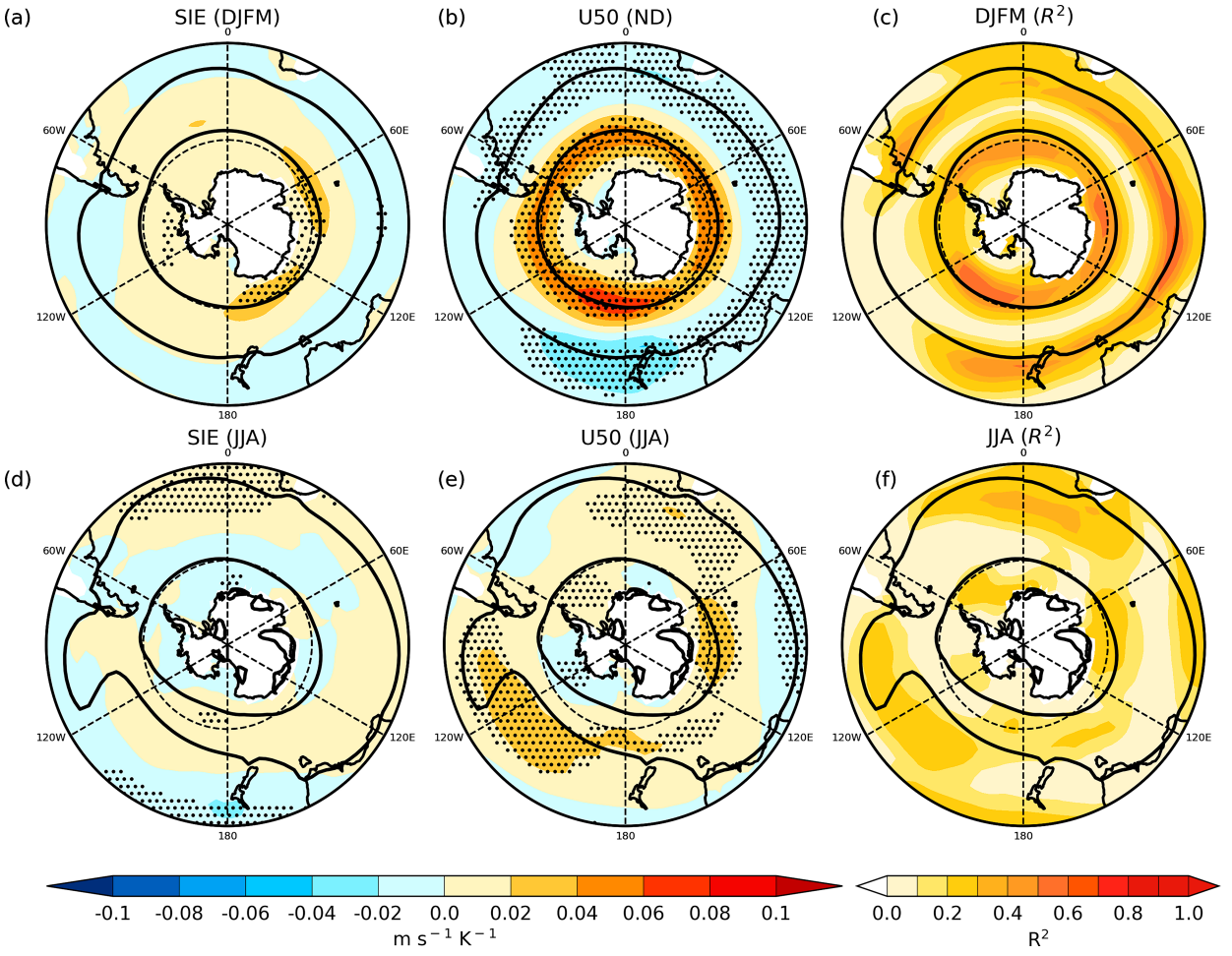


FIG. 3. The sensitivity of global warming scaled U850 (m s$^{-1}$ K$^{-1}$) associated with the uncertainty in the future SIE loss and SPV strengthening response, according to SSP5-8.5, as determined using each MLR model [Eqs. (1) and (2)]; expressed for a 1$\sigma$ positive anomaly in projected (a) SIE loss and (b) SPV strengthening (change in $U50_{ND}$) according to the multimodel CMIP6 ensemble spread, together with (c) the MLR model explained variance ($r^2$) for summer. (d)–(f) The results for winter. Statistical significance at the 95% level ($p < 0.05$) is indicated using stippling in (a), (b), (d), and (e). The black solid line denotes the seasonal mean 8 m s$^{-1}$ wind contour during the historical period (1940–69).

more different (Figs. 3d,e). A lack of statistical significance is evident for the SIE loss term in this season, largely in contrast to summer, with only a slight overall positive sensitivity (increase in U850 with weaker SIE loss) evident in the region of the climatological-mean jet position (exceeding 8 m s$^{-1}$). The sensitivity is overall more positive in response to a 1$\sigma$ change in U50 but with significant spatial variability. The response in U850 to the U50 predictor is largest and statistically significant between 60° and 120°E, adjacent to the coast (Davis Sea), and between 90° and 150°W for the latitude range ~35°–50°S (South Pacific sector), with statistical significance also apparent in the Weddell Sea and southward of South Africa. An $r^2$ value of >0.2 (20% explained variance) is again apparent over these regions, locally exceeding 0.3 (30% explained variance) south of South Africa (~40°–50°S). This finding confirms that the two chosen remote drivers explain less variance in winter, which contrasts with that shown in M20 (Fig. 11), implying a potentially more significant role of upper tropospheric TW during this season. This is confirmed from Figs. S6c and S6d, with strongest sensitivity mainly but not exclusively at lower latitudes (such that TW does appear to be more important as a driver for Antarctic climate response in this season). The total explained variance in U850 is still modest even when all three predictors are included, which may point to the importance of teleconnections in influencing zonal asymmetries in U850 during winter. The strength of the physical relationships may, however, be underestimated due to model deficiencies that warrant further investigation.

### 3) STATISTICAL DERIVATION OF STORYLINES

To obtain each storyline, the regression coefficients ($b_x$ and $c_x$) derived in Eqs. (1) and (2) were multiplied by a storyline coefficient ($S$). Following Zappa and Shepherd (2017), the

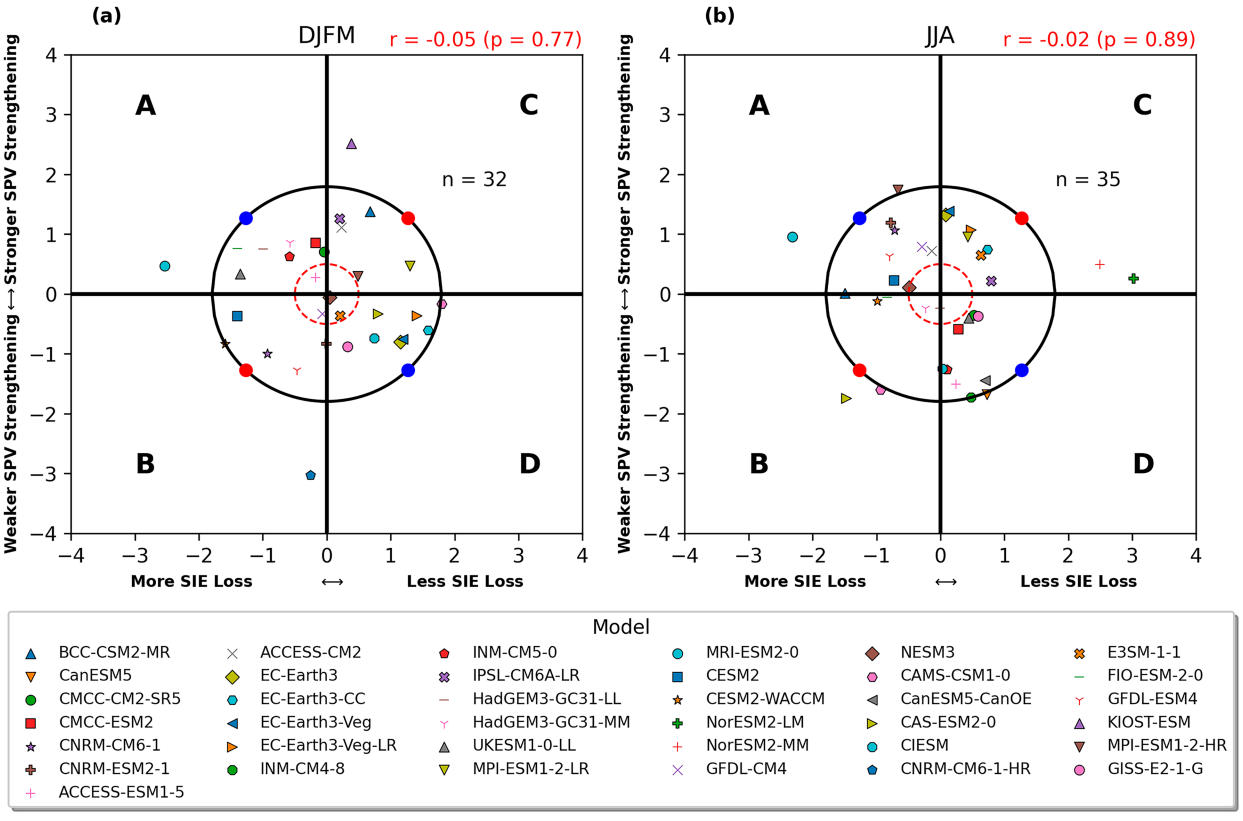


FIG. 4. Distribution of the normalized (scaled by global warming) and standardized model responses for SSP5-8.5 of each remote driver ($x$ axis: SIE loss and $y$ axis: SPV strengthening expressed as $\sigma$ from the multimodel mean response) for the extended austral summer and winter seasons. Note that negative values of anomalous SIE loss correspond to stronger SIE loss than the multimodel mean and vice versa. The black solid lines correspond to the multimodel mean change for each respective driver and the joint fitted 80% confidence ellipse of the $\chi^2$ distribution (with two degrees of freedom) is overlaid as in M20. The extreme (intermediate) storyline positions are shown as red (blue) points located along the ellipse (equidistant from the center point). Symbols used to represent the models are provided in the legend. In each case, both predictors are statistically uncorrelated with each other across all models, according to a two-sided $t$ test as indicated (top right). In each panel, the quadrants are labeled (A, B, C, D) in accordance with which storylines they represent. Note that we consider models with standardized anomalies of <0.5 for both predictors as unrepresentative of any particular storyline (within the inner red dashed ellipse).

coefficient is chosen to correspond to the 80% confidence region of the joint distribution in the two remote drivers as shown in Fig. 4. For a pair of uncorrelated predictors, after scaling by global warming, the storyline coefficient takes the value of ~1.26 (see appendix A in M20 for details). Equation (3) describes the mathematical derivation of four plausible storylines using the constructed seasonal MLR models, fitted using data from the suite of CMIP6 models included:

$$P_x = a_x \pm b_x S \pm c_x S. \tag{3}$$

The term $S$ is multiplied by each regression coefficient ($b_x$ and $c_x$) at each grid point and added/subtracted from the multimodel mean response of the given target variable $a_x$ to derive four plausible storylines of the pattern of response ($P_x$), according to the following:

1) High SIE loss (+) and strong SPV strengthening (+)
2) High SIE loss (+) and weak SPV strengthening (−)
3) Low SIE loss (−) and strong SPV strengthening (+)
4) Low SIE loss (−) and weak SPV strengthening (−)

Note that the + and − correspond to addition and subtraction, respectively, of terms $b_xS$ and $c_xS$ in Eq. (3) and the lettering to each storyline, labeled in Fig. 4 in each respective quadrant. The standardized distribution of the scaled predictor responses for all included CMIP6 models, centered around the multimodel mean change in SIE loss and SPV strengthening, is displayed in Fig. 4 for summer and winter. We refer to storylines B and C (red dots in Fig. 4 located along the ellipse) as "extreme" storylines, where the standardized projected change in each driver is opposite in sign with respect to the multimodel mean, are evaluated where the hypothetical line $(\Delta\text{SIE}/\Delta T)' = (\Delta\text{SPV}/\Delta T)'$ intersects with the ellipse. By contrast, storylines A and D (blue dots in Fig. 4 located along the ellipse) are labeled as "intermediate" storylines, where the standardized driver response is equal in sign relative to the multimodel mean, correspond to the intersection of the ellipse

and hypothetical line $(\Delta SIE/\Delta T)' = -(\Delta SPV/\Delta T)'$. The reasoning for the above labeling of extreme and intermediate storylines is evident from sections 3 and 4, in that storylines B and C are typically most contrasting, except for precipitation. This is because enhanced SPV strengthening combined with reduced SIE loss (and vice versa) drive changes in U850 (jet response) and Antarctic temperature in the same direction. While the spread of the model scaled predictor responses is largely randomly distributed (as expected by design if each chosen driver is uncorrelated across all models which we confirm in each case), the number of models most representative of each storyline is highly variable. Thus, a unique model solution that best represents a storyline is lacking in some cases, whereas multiple candidate models exist for others.

For the subsample of models with five or more individual realizations (using a consistent model physics and forcing variant) available for SSP5-8.5 (Table S1), the sensitivity of the results to internal variability was determined to be small (Fig. S1). This finding is not unexpected when considering that SSP5-8.5 simulations are influenced by a very large induced radiative forcing and justifies the decision to concentrate on this most extreme, albeit unlikely, scenario in being able to discern model relationships of midlatitude jet (atmospheric circulation) response contingent on both the magnitude of SIE loss and SPV strengthening. The lack of sensitivity to internal variability would be consistent with other studies that have found that model uncertainty dominates the total uncertainty, as noted in projections of the Arctic SPV for example (Karpechko et al. 2022). Although model agreement exists for an overall strengthening and later spring breakdown of the SH SPV by the end of the century across models, at least due to the GHG effect (e.g., M20), model uncertainty can be expected to dominate over internal variability due to the competing effects of ozone recovery. This is strongly linked to model representation of stratospheric ozone, including resolution of zonal asymmetries (Waugh et al. 2009), and the realism of simulated radiative–dynamical interactions (e.g., Revell et al. 2022). Given also that most models had fewer than five available realizations, subsequent results shown were derived using only the first available realization.

### d. Model historical performance score

In providing a recommendation of models most representative of each storyline, a scoring metric was defined to categorize models based on the performance of the historical simulations with respect to ERA5, for the following variables:

1) U50 (50°–60°S): November–December (ND)/JJA
2) SH SIE: DJFM/JJA
3) T2m (50°–90°S): DJFM/JJA
4) U850 (40°–70°S): DJFM/JJA

The first two variables are the storyline predictors, while the latter two were considered key variables of focus in this study in assessing the midlatitude jet response and amount of Antarctic warming, with implications for a wide range of physical and biogeochemical processes relevant to key features of the Southern Ocean (e.g., Antarctic Circumpolar Current).

Both an area-weighted root-mean-square error (RMSE) [Eq. (4)] and a normalized interannual variance metric ($\sigma^2_{\text{Norm}}$) [Eq. (5)] was considered for variables U50, T2m, and U850:

$$\text{RMSE} = \sqrt{\sum_{x=1}^{m} w_x(\text{MOD}_x - \text{OBS}_x)^2}, \tag{4}$$

$$\sigma^2_{\text{Norm}} = \sum_{x=1}^{m} w_x\left(\frac{\sigma^2_{\text{MOD}} - \sigma^2_{\text{OBS}}}{\sigma^2_{\text{OBS}}}\right), \tag{5}$$

where MOD refers to model and OBS refers to ERA5. For $m$ models, using a field of grid points $x$, the area-weighted ($w_x$) sum of the squared difference of climatological values of the field over the 1985 to 2014 period, for each month, was computed between each model and ERA5 in Eq. (4). The term $\sigma^2_{\text{Norm}}$ was calculated in a similar manner for all years $j$ between 1985 and 2014 [Eq. (5)]. For SIE, the IIEE [as formulated in Goessling et al. (2016)] was used instead of RMSE, with variance calculated over all 30 years (the spatial aspect is already factored in when calculating IIEE) for the normalized IIEE [calculated in Eq. (S1)].

The mean and standard deviation ($\sigma$) was then subsequently computed over all model values. To objectively classify models according to their overall performance, a tolerance threshold was calculated for each variable and metric: set as the mean + 1$\sigma$ (4 variables × 2 metrics = 8 tests). Models within each limit received a score of 1, corresponding to a pass of each test. Conversely, models outside this limit received a 0, denoting a failed test. This equates to a failure rate of ~16% of all models for a given test (assuming a Gaussian distribution). The scores were summed to provide an overall grade for each model (maximum score of 8). As the majority of models (~two-thirds) received a score of either 7 or 8, the discrimination between models that fail only one test was further enhanced by categorizing the subset of models that failed a predictor test (for U50 or SIE) below those that failed a nonpredictor test (for T2m or U850); we expressed the score for the latter subset as 7*. Results are shown in Table S2 (summer) and Table S3 (winter), and in Fig. 5.

### e. Candidate models for representing storylines

In identifying candidate models most representative of the different storylines that could be selected to further investigate regional impacts, the results of implementing the straightforward scoring approach are shown here for each set of storylines. The predictor response diagram (Fig. 4) is repeated in Fig. 5, color coded according to the overall model grade received. Models most representative of each storyline accounting for both distance from the optimum storyline position and historical performance grade are listed in Table 2. For each storyline, at least one model is identified as having a score of 7 (one test failed) or 8 (all tests passed). Confidence was thus ensured that all storylines can be represented by

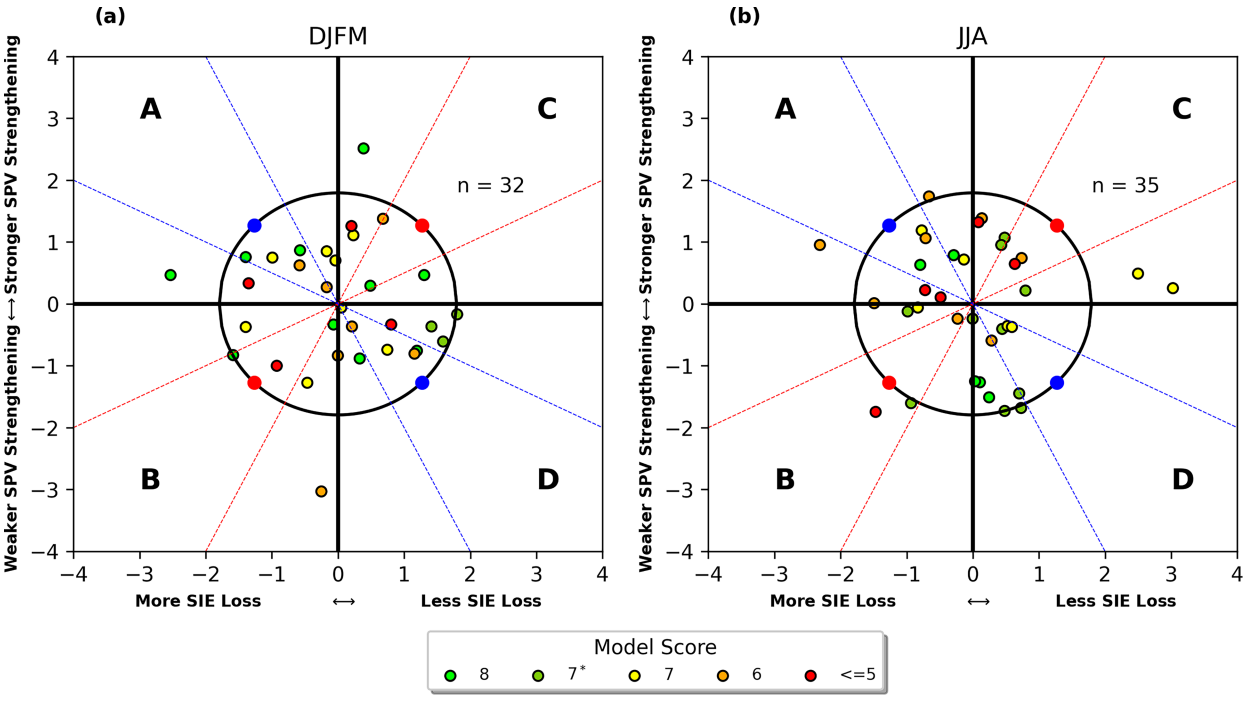


FIG. 5. As in Fig. 4, but the colors for each model denote the performance of the historical simulations using the two predictor variables, U50 (50°–60°S) and SH SIE, together with the two nonpredictor variables, T2m (50°–90°S) and U850 (40°–70°S). The identified candidate models most representative of each storyline reside within the two dotted lines in each quadrant and are listed in Table 2, albeit with a couple of exceptions. The total score corresponds to the overall number of failed tests (i.e., score of 8 = all test passed, 7 = one test failed etc.). The 7* denotes models that fail a single nonpredictor test; these models are categorized ahead of those that fail a predictor test (score of 7).

models that are suited for applications such as dynamical downscaling.

## 3. Results: Summer

Storyline results are here shown for summer, centered around the multimodel mean response, for the following target variables: 850-hPa zonal wind (U850), 2-m surface air temperature (T2m), and precipitation (including both large-scale and convective partitions). The results are expressed as the mean climatological response per degree of global warming, according to SSP5-8.5. In each case, storylines B and C represent the extreme storylines and storylines A and D represent the intermediate storylines. In assessing the relationship between the midlatitude jet and Antarctic climate response, we quantify storyline changes in both jet strength (JSTR) and

TABLE 2. Candidate GCMs from the suite of CMIP6 models most representative of each storyline, centered around each of the four storylines for each season (summer and winter; Figs. 4 and 5). Models in which all eight tests were passed receive a score of 8; with a score of 7* for all models failing only one nonpredictor test, 7 for all models failing only one predictor test, 6 if two tests are failed, and ≤5 for a few remaining models failing three or more tests. See Tables S2 (summer) and S3 (winter) for a detailed breakdown of the assigned overall performance grade for each model and specific tests failed. Storylines B and C (bold font) are highlighted as they were later found to be typically most contrasting for dynamically sensitive variables: U850 and T2m. Note models with a caret (^) are outside the region between the two dotted lines in Fig. 5 but are included as candidates due to their much closer proximity compared with the alternative suggested model for each of the affected storylines.

| | | | DJFM | | JJA | |
|---|---|---|---|---|---|---|
| Storyline | SIE loss (+ or −) | SPV (+ or −) | Model | Score | Model | Score |
| A | + | + | FIO-ESM2-0 | 8 | GFDL-ESM4 | 8 |
| | | | HadGEM-GC31-MM | 8 | CNRM-CM6-1 | 8 |
| **B** | **+** | **−** | **CESM2-WACCM** | **8** | **CAMS-CSM1-0** | 7* |
| | | | **CESM2** | **7** | | |
| **C** | **−** | **+** | **MPI-ESM1-2-HR** | **8** | **MPI-ESM1-2-LR** | 7* |
| | | | **MPI-ESM1-2-LR^** | **8** | | |
| D | − | − | EC-Earth3-Veg | 7* | UKESM1-0-LL | 8 |
| | | | CIESM | 7 | CanESM5-CanOE^ | 8 |

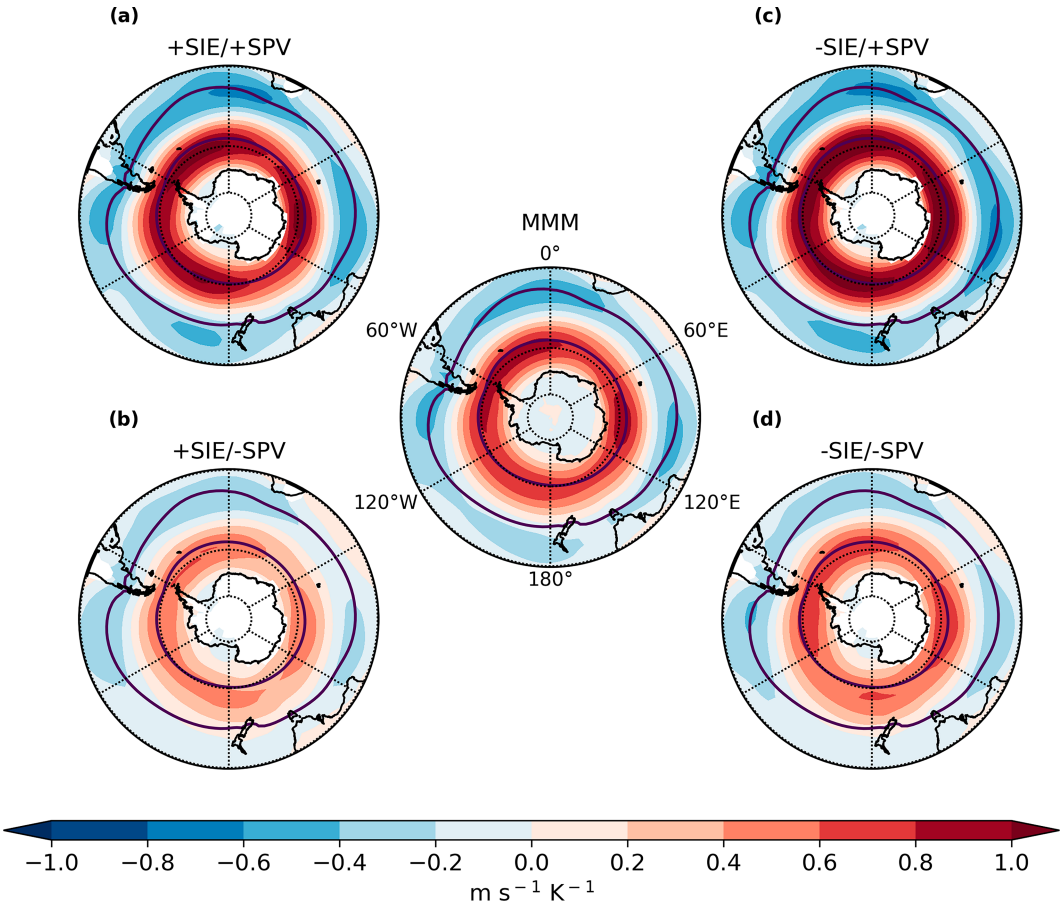


FIG. 6. Scaled mean storyline responses in summer climatological-mean U850 (m $s^{-1}$ $K^{-1}$) between 2070 and 2099 (future) and 1940–69 (historical), according to SSP5-8.5, are shown for each of the four storylines corresponding to (a) high SIE loss (+)/strong SPV strengthening (+), (b) high SIE loss (+)/weak SPV strengthening (−), (c) low SIE loss (−)/late strong SPV strengthening (+), and (d) low SIE loss (−)/weak SPV strengthening (−). The results are shown centered around the multimodel mean (MMM) scaled response to illustrate variance in the projected pattern, conditional upon both the magnitude of SIE loss and SPV strengthening. The solid indigo lines denote the climatological-mean 8 m $s^{-1}$ U850 wind contour during the historical period, as an indicator of the jet position.

jet position (JPOS), following the approach of Bracegirdle et al. (2018).

### a. U850 response

Due to the land–ocean distribution in the SH, changes in climate often manifest in a largely zonally symmetric pattern. As discussed earlier, the eddy-driven jet is a key feature sensitive to climate change and is influenced strongly by the timing of the seasonal breakdown in the SPV, together with the overall extent and geographical distribution of Antarctic sea ice. As shown in Fig. 6 and confirmed from Table 3 for summer, the tropospheric jet is projected to both strengthen and shift poleward due to climate change (a robust feature of climate model projections) according to both the multimodel mean and the four derived storylines using these two established drivers. Overall, when comparing storyline pairs associated with equivalent SPV strengthening (A versus C and B versus D), the ΔJSTR is slightly greater for the two storylines with weaker SIE loss (storylines C and D) but with negligible difference in ΔJPOS values. When comparing storylines with the same amount of SIE loss (A versus B and C versus D), the ΔJSTR response is also more pronounced between the two

TABLE 3. Calculated storyline changes (units of per °C of global warming) in jet strength (JSTR) and jet position (JPOS) for summer, using the jet diagnostics defined in Bracegirdle et al. (2018).

| Storyline | ΔJSTR (m $s^{-1}$ $K^{-1}$) | ΔJPOS (° $K^{-1}$) |
|---|---|---|
| A: High SIE loss/strong SPV strengthening | 0.300 | −0.815 |
| B: High SIE loss/weak SPV strengthening | 0.195 | −0.410 |
| C: Low SIE loss/strong SPV strengthening | 0.386 | −0.836 |
| D: Low SIE loss/weak SPV strengthening | 0.281 | −0.431 |

storylines characterized by a weak SPV strengthening (storylines B and D) versus a strong SPV strengthening (storylines A and C). In terms of the ΔJPOS, storylines A and C are characterized by approximately a doubling of the zonally averaged mean-state poleward shift in the jet relative to storylines B and D by the end of the century. For storylines A and C, the change in U850 widely exceeds 1 m $s^{-1}$ $K^{-1}$, with a calculated ΔJSTR of ~0.3–0.4 m $s^{-1}$ $K^{-1}$ and ΔJPOS of ~0.80°–0.85° $K^{-1}$. When rescaling upward such numbers by a typical global warming value for each storyline, these values correspond to around approximately +1.5–2 m $s^{-1}$ (ΔJSTR) and from around −3° to −4° (ΔJPOS). This is shown in Fig. S7, where the distributions are aggregated for all models in each respective storyline quadrant and changes computed for all 30 years to yield a statistically large sample size in verifying the robustness of these storyline differences.

The stronger U850 (jet) response for storylines A and C, associated with a delayed deceleration of the SPV (U50) earlier in the season, can be understood in terms of a postponed influence into the troposphere via stratosphere–troposphere coupling, with a typical 1–2-month lag (Sun et al. 2014). The somewhat larger response in jet strengthening for relatively weaker SIE loss is conversely more complicated to understand. Bracegirdle et al. (2018) found that around 40% of the variance in SH projected jet strengthening could be attributed to model diversity in simulated historical sea ice area in austral summer (DJF), using CMIP5 models for a representative concentration pathway scenario corresponding to an increased radiative forcing of 8.5 W $m^{-2}$ by 2100 (RCP8.5; van Vuuren et al. 2011a). However, the physical robustness of this relationship was cast into doubt in their study as evidence from atmosphere-only studies implied a negligible impact on tropospheric circulation (e.g., Raphael 2003; Kidston et al. 2011). Models with greater coverage of sea ice in the historical period are typically characterized by larger sea ice loss into the future and subsequently less jet strengthening as the lower tropospheric meridional temperature gradient is weakened around Antarctica (Bracegirdle et al. 2018). This is consistent with earlier intermodel comparison studies, with ramifications for the degree of Antarctic warming (Flato 2004; Bracegirdle et al. 2015). This relationship is known as an emergent constraint (Collins et al. 2012) in which historical biases or trends are related to future trends; derived empirically when using a large suite of climate model output to assess future projections.

### b. T2m response

The summer storyline responses in T2m for each storyline and the multimodel mean are shown in Fig. 7. The response is more zonally symmetric for storylines C and D versus A and B (greater warming equatorward of 50°S, as well as over the Antarctic continent), which are characterized by weaker SIE loss (although not necessarily associated with more remaining SIE in the future due to the aforementioned emergent relationship). For storyline C, regions over or adjacent to the sea ice margin in the historical period are characterized by a very subdued change in T2m of less than 0.5 K $K^{-1}$. The subdued surface warming for this storyline in particular, which also emerges for SSTs (not shown), might be related to equatorward Ekman transport as a result of the amplified jet strengthening (+SAM) response. Although studies have postulated such response to anthropogenic climate change as a short-term response, which is subsequently negated by sustained upwelling and associated warming on decadal time scales, Doddridge et al. (2019) found indications from model experiments that this process may be overridden by an eddy compensation mechanism that could act to oppose the long-term upwelling signal.

Values between 0.5 and 1.0 K $K^{-1}$ are typical north of 50°S and over the Antarctic continent for both storylines C and D, which although larger is still below the global average rate of warming (equal to 1.0 K $K^{-1}$ by definition). The rate of warming according to these storylines is likely limited by the strong thermal inertia of the Southern Ocean as well as the buffer that is provided by sea ice coverage and a stronger zonal circulation (Stouffer 2004; Xie et al. 2010; Yin et al. 2011; Li et al. 2013). In contrast, storylines A and more especially B show a T2m increase widely in excess of 1.0 K $K^{-1}$ over a large swath of the Antarctic continent, with a more uniform rate of warming for the area equatorward of ~50°S (particularly storyline B) slightly below the global average (~0.6–1.0 K $K^{-1}$). The pattern of T2m response across storylines appears to be inversely related to the magnitude of simulated tropospheric jet strengthening, as discussed previously, with a smaller contribution from the relative amount of sea ice loss in the future. Comparing both extreme storylines B and C, an increase in jet strength ranging from ~0.2 to nearly 0.4 m $s^{-1}$ $K^{-1}$ (Table 3) translates to >1.2 and <0.6 K $K^{-1}$ of warming respectively for storylines B and C over the Antarctic continent. Thus, the storylines generated here show that there is a factor of 2 difference between the degree of tropospheric jet strengthening and the resultant warming over Antarctica, according to the selected set of CMIP6 models used here in the storyline analysis, contingent on SIE loss and SPV strengthening. Despite the storyline pairs with equal SPV strengthening displaying similar ΔJPOS (the poleward jet shift is approximately double that for A and C compared to B and D; Table 3), the difference in Antarctic warming is smaller for storyline pairs with equivalent SIE loss (stronger Antarctic warming with more SIE loss in A and B and weaker warming with less SIE loss in C and D; Fig. 7). This highlights the importance of SIE loss in modulating Antarctic warming, which may be amplified through ΔJSTR but appears to be highly insensitive to projected ΔJPOS. As much as ~30%–40% explained variance in T2m change can be attributed to both predictors over west Antarctica (~20%–30% elsewhere), with greater sensitivity to the SPV predictor and SIE loss predictor over West and East Antarctica respectively (Figs. S8a–c).

### c. Precipitation response

The pattern of the summer response in precipitation for the multimodel mean response and each of the SH storylines is shown in Fig. 8. As for U850 (Fig. 6) the response is qualitatively very similar around Antarctica for each scenario, in that a circumpolar increase in precipitation is expected between ~55° and 70°S. This is likely connected with a stronger jet

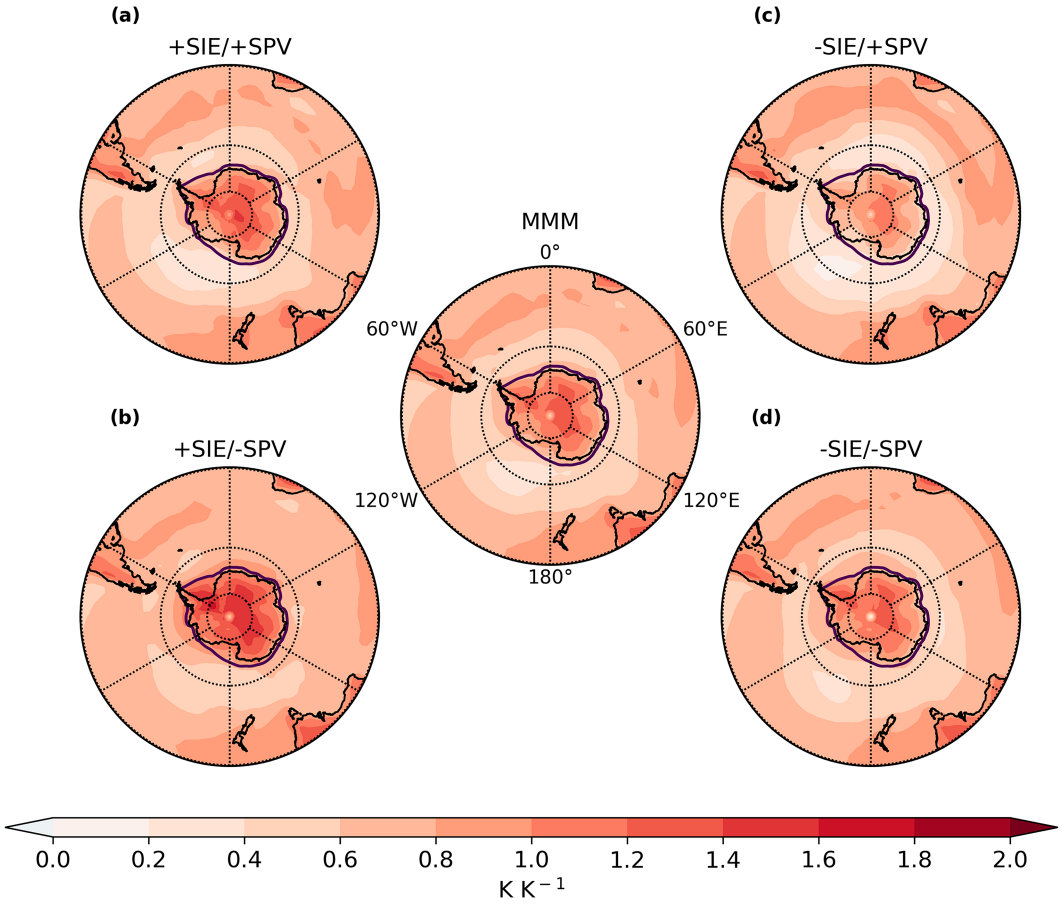


FIG. 7. As in Fig. 6, but for the projected responses in T2m (K $K^{-1}$). The solid indigo lines denote the −1.8°C isotherm to demarcate the approximate location of the climatological-mean sea ice edge during the historical period.

promoting cyclonic conditions, in conjunction with background warming leading to an increase in the water vapor holding capacity of the atmosphere (i.e., ~7% per 1°C warming according to the Clausius–Clapeyron relation). The pattern of response over midlatitude regions is, conversely, highly variable for each storyline, as was also found in M20; regional patterns are largely consistent in sign just not magnitude (e.g., drying over southernmost western South America and wetting along the western coast of the Antarctic Peninsula). The strongest overall response is shown for storyline A (~0.1–0.2 mm $day^{-1}$ $K^{-1}$), with a much weaker signal for storyline D (<0.1 mm $day^{-1}$ $K^{-1}$). A drying response is suggested at lower latitudes (~35°–50°S) for regions corresponding with the climatological centers of subtropical high pressure systems, most prominent for storylines A and C (from ~−0.1 to −0.2 mm $day^{-1}$ $K^{-1}$), as is consistent with the hemispheric zonal wave 3 pattern (Goyal et al. 2021; Campitelli et al. 2022). The more pronounced midlatitude drying for these two storylines, characterized by greater SPV strengthening, implies a stronger effect from the much larger poleward shift (>0.8° $K^{-1}$) of the jet for these two storylines relative to storylines B and D (<0.45° $K^{-1}$) (Table 3). This assertion is made on the basis that the jet strengthening is somewhat larger for storyline C (0.386 m $s^{-1}$ $K^{-1}$) compared with A (0.300 m $s^{-1}$ $K^{-1}$), and yet both the pattern and magnitude of high-latitude wetting and midlatitude drying are difficult to distinguish.

In terms of modulating the high-latitude wetting and midlatitude drying response, the influence is statistically significant only for the SPV strengthening (U50) predictor, yielding comparable explained variance (up to ~30%–40%) as for the T2m change during this season (Figs. S8d–f). It is important to note that intermediate storylines A and D are most contrasting for this variable, in comparison to extreme storylines B and C for U850 and T2m (shown also in Fig. S9). This likely reflects both the role of lower-tropospheric moistening due to SIE loss and enhanced baroclinicity around Antarctica in association with a strengthening and poleward shift of the jet, serving to promote greater extratropical cyclone activity (e.g., Simmonds et al. 2003), in influencing high-latitude precipitation response around Antarctic during this season.

## 4. Results: Winter

Storylines of winter U850, T2m, and precipitation response, according to the relative amount of SIE loss and SPV strengthening across the range of CMIP6 models included,

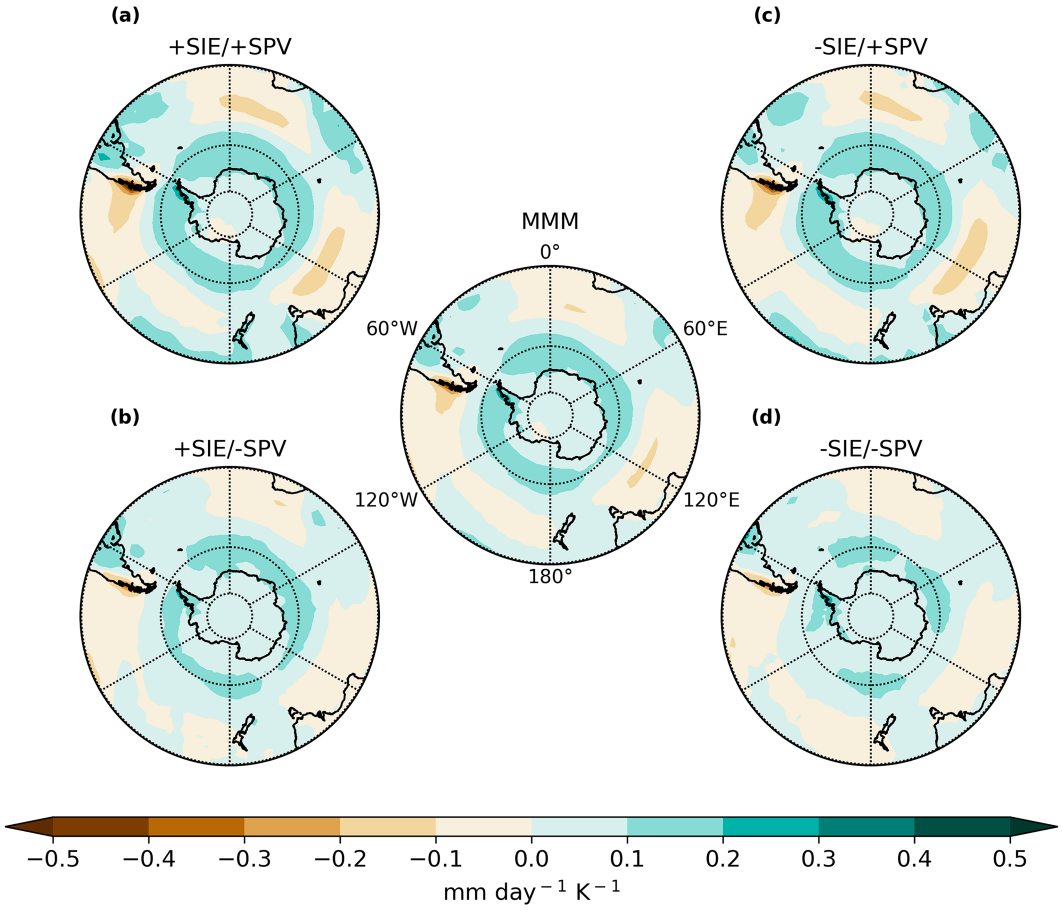


FIG. 8. As in Figs. 6 and 7, but for the projected responses in precipitation (mm day$^{-1}$ K$^{-1}$).

are subsequently shown here. Given the notably lower amount of explained variance in U850 (jet) response for this season (~35% as opposed to ~70% in summer; Fig. 3), we must caution against the realism of any such storyline physically materializing. Nevertheless, the results are still important in helping to disentangle and quantify the relative influence of each remote driver on the midlatitude jet and Antarctic climate response.

### *a. U850 response*

The response in U850 for winter is shown in Fig. 9. While the pattern of the response is less zonally symmetric than for summer (Fig. 6), the response is largely qualitatively consistent between each of the four storylines. Storylines B and D indicate less overall strengthening of the tropospheric jet during this season, notwithstanding some significant regional disparities, with ΔJSTR values of 0.252 and 0.321 m s$^{-1}$ K$^{-1}$ respectively (Table 4). Storylines A and C show a more pronounced strengthening of the tropospheric jet between 60°E eastward to 120°W (~0.5–1.0 m s$^{-1}$ K$^{-1}$ for storylines A and C near to 50°S), with zonally averaged (ΔJSTR) values of 0.403 and 0.471 m s$^{-1}$ K$^{-1}$ respectively. Although storylines B and D are characterized by a much weaker response, significant longitudinal variation is apparent (typically <0.5 m s$^{-1}$ K$^{-1}$).

Concerning storyline variations in ΔJPOS, we note that storylines A and D are most contrasting, with up to a factor of 3 difference (values of −0.161° and −0.442° K$^{-1}$ respectively). In fact, the role of SIE loss (comparing storylines A versus C and B versus D) exceeds that of SPV strengthening (comparing storylines A versus B and C versus D) in terms of modulating the poleward shift of the jet (~62% versus 38% respectively, as calculated by differencing the values in Table 4). We note that the values presented here need to be multiplied by a representative global warming value to capture the true magnitude projected changes suggested according to CMIP6 models. As shown from Fig. S10, these variations in jet response across storylines are robust and consistent when factoring in all models and accounting for all years in the respective historical and future periods.

### *b. T2m response*

In winter, when sea ice extends far from the continental margin, a sharp gradient in the magnitude of warming is apparent for both the multimodel mean response and each storyline (Fig. 10) close to the sea ice margin (−1.8°C

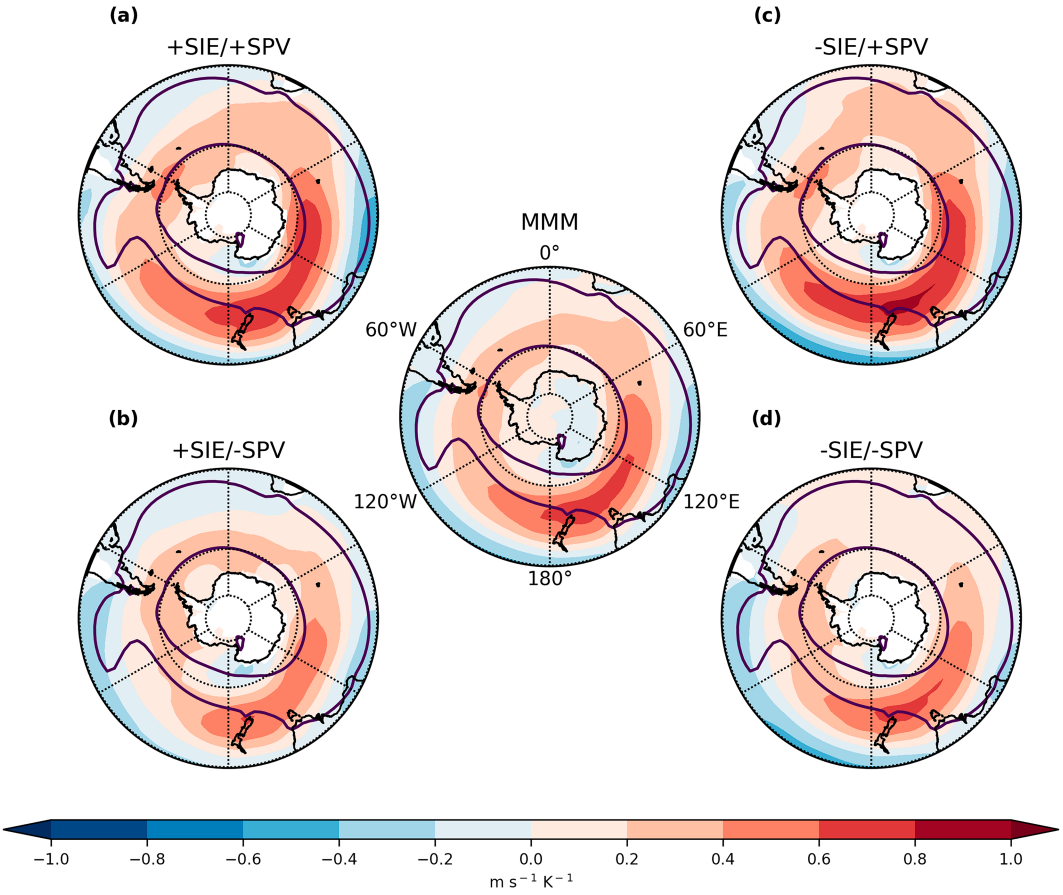


FIG. 9. As in Fig. 6, but for winter.

isotherm), most pronounced for storyline B and least pronounced for storyline C. As for summer, the difference in warming seems to be more connected with the ΔJSTR as opposed to ΔJPOS (Table 4). Geographically, the magnitude of warming is maximized over the coastal seas of Antarctica, and more particularly in the Western Hemisphere. In essence, much of the Antarctic is projected to warm by a larger amount in this season compared with the global average (values greater than 1 K $K^{-1}$), as the energy imbalance in the climate system translates exclusively to sensible heating over these regions. This is associated with a direct increase in the ambient air temperature in the absence of phase changes (melting of snow and ice or evaporation over open ocean) during the long polar night. Hence, the pattern of warming contrasts with the surrounding, sea ice free region of the Southern Ocean where latent heating becomes important (damping the increase in ambient air temperature). Nevertheless, the relatively smaller increase in surface air temperature over land relative to the adjacent seas is testament to the buffer that sea ice (at least historically) is likely to exert in the future winter climate, particularly but not exclusively over western Antarctic which is evident to some degree for all storylines (Fig. 10). It is confirmed from Figs. S11a–c that T2m is highly sensitive to both predictors over sea ice affected regions and a weaker statistically significant signal extends to midlatitudes, resulting in explained variance on the order of ~20%–40% widely over the Southern Ocean, which is larger than that shown for summer (Fig. S8c).

TABLE 4. As in Table 3, but for winter (JJA).

| Storyline | ΔJSTR (m $s^{-1}$ $K^{-1}$) | ΔJPOS (° $K^{-1}$) |
|---|---|---|
| A: High SIE loss/strong SPV strengthening | 0.403 | −0.442 |
| B: High SIE loss/weak SPV strengthening | 0.252 | −0.336 |
| C: Low SIE loss/strong SPV strengthening | 0.471 | −0.267 |
| D: Low SIE loss/weak SPV strengthening | 0.321 | −0.161 |

Similar to summer, the rate of T2m increase equatorward of ~55°S is below the global average for all four storylines. This is more pronounced for storyline C (ranging between ~0.2 and 0.6 K $K^{-1}$) with the lowest values just equatorward of the sea ice edge, particularly north of the Ross Sea. A more uniform pattern is shown for storyline B (~0.6–1.0 K $K^{-1}$) as noted previously for summer (Fig. 7). This contrast

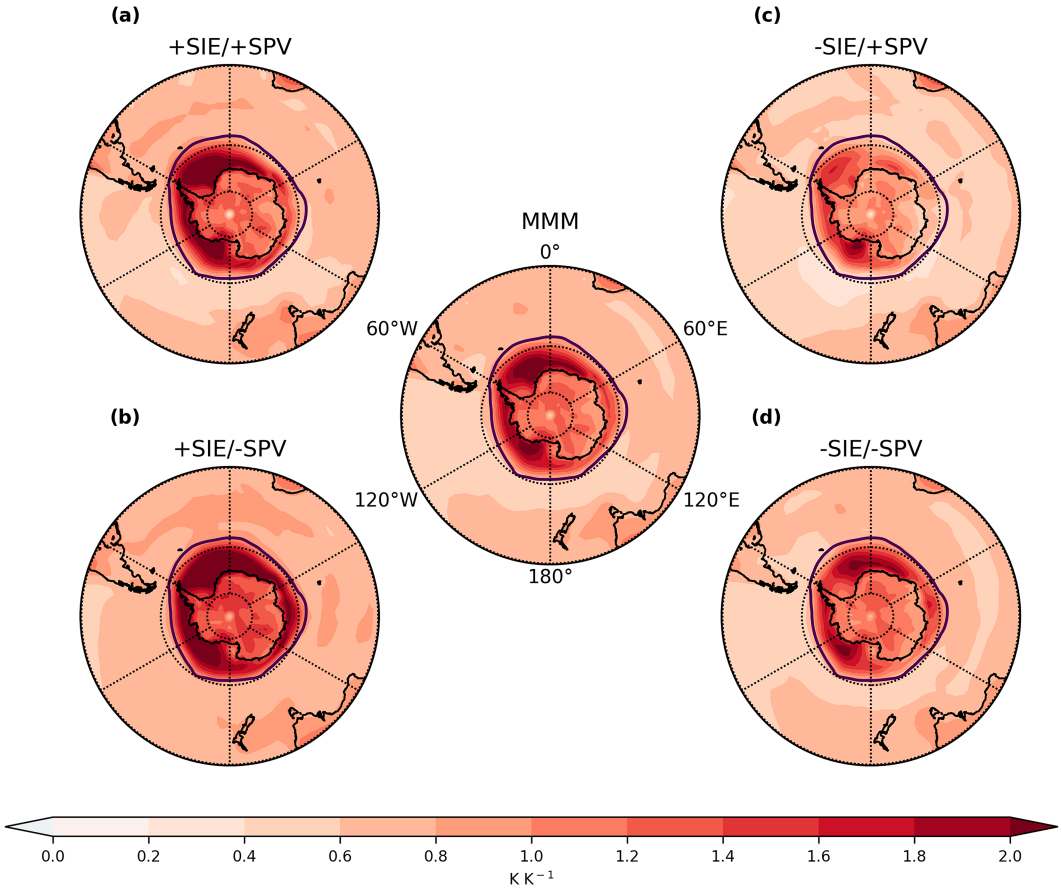


FIG. 10. As in Fig. 7, but for winter.

demonstrates that storylines with a stronger increase in the tropospheric jet are associated with a reduced sharpness in the temperature discontinuity associated with the sea ice edge. For instance, Storyline C (associated with the largest projected ΔJSTR) shows a smaller difference between open ocean and ice-covered regions as mixing of air from lower latitudes (warm air advection) is reduced, particularly along the East Antarctic coastline. In terms of the differences between storylines, storylines B and C are again most contrasting, except for the ΔJPOS which we interpret from Fig. 10 to have a much smaller influence on Antarctic warming spatial response. This serves to highlight the counteracting effects of SIE loss and SPV strengthening over the magnitude of projected warming across Antarctica.

### c. *Precipitation response*

In Fig. 11, the precipitation response for winter is shown. The overall tendency in precipitation change is again consistent with that shown earlier for summer (Fig. 8), although the circumpolar increase in precipitation over the southernmost Southern Ocean shows greater longitudinal variability and extends further equatorward. Equatorward of 40°S, a more coherent (zonally continuous) midlatitude drying response is evident compared to summer. This is broadly consistent with the corresponding U850 storyline responses for this summer (Fig. 9). The high uncertainty in lower-latitude precipitation projections is inherent due to the enhanced sensitivity of this variable to dynamical influences, driven by internal atmospheric variability (Deser et al. 2012), which can only partially be captured in a storyline framework. However, it should be noted that the remote drivers considered here are relatively unimportant in attempting to understand model uncertainty in low-latitude precipitation using the storyline approach, relative to other features such as upper-tropospheric TW that have a demonstrably strong influence (e.g., M20). This is reflected by the insensitivity to either predictor and the low explained variance across much the SH extratropics (Figs. S11d–f). In contrast, the precipitation response poleward of 50°S is largely subject to thermodynamic control and subsequently the uncertainty in response is much weaker (IPCC 2022), as is indeed shown here.

Although less pronounced compared to summer, storylines A and D are most contrasting for this variable (Fig. S12), at least for the west Antarctic region, with a general wetting over the Southern Ocean ranging between ~0.1 and 0.3 mm $day^{-1}$ $K^{-1}$. The imprint on the precipitation response from the zonal wave-3 pattern is less evident for this season at lower latitudes, likely due to an equatorward shifted zonal circulation with respect

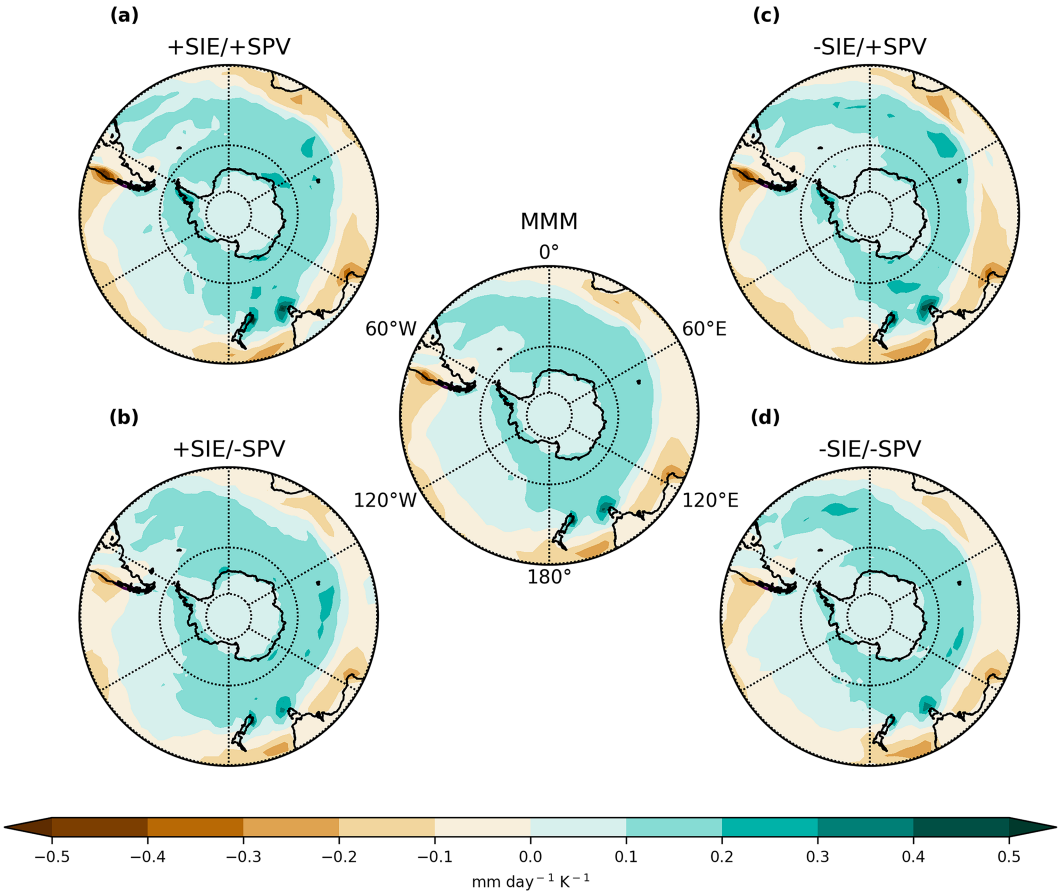


FIG. 11. As in Fig. 8, but for winter.

to summer during this season, with a general drying response evident equatorward of 40°S. An interesting contrast again apparent for this season is the drying response along the western coast of South America ($<-0.5$ mm day$^{-1}$ K$^{-1}$) versus a wetting response along the western Antarctic Peninsula ($>0.2$ mm day$^{-1}$ K$^{-1}$) for storyline A. This bimodal response is likely a function of the projected shift toward a positive-phase SAM, which is further amplified by the orographic effect provided by the Andes and mountainous Antarctic Peninsula. This tendency is indeed qualitatively consistent for all four storylines but much less pronounced for storyline D. Additionally, there is more coherent spatial structure in the precipitation response for storylines C and D, as well as the MMM response, which is coincident with the climatological positioning of the wintertime jet (entrance region over the South Atlantic between ~35° and 45°S that migrates poleward in latitude as the jet transits longitudinally eastward, with an exit region along the western coast of the Antarctic peninsula; Williams et al. 2007).

## 5. Discussion

This study highlights the merit of using a storyline approach, using the current generation of CMIP6 climate models, to assess the relative influence of wintertime SPV strengthening/summertime vortex breakdown delay versus SIE decline on the midlatitude jet and in turn the regional response of the near-surface climate for the Antarctic. This framework helps to illustrate the range in uncertainty across climate model projections and furthers our understanding of the processes involved in determining the large intermodel spread. Communicating uncertainty in climate model projections is needed not only to further advance global and regional climate modeling, but also to support interpretation of the impacts of future polar climate change on the Earth system and society. This information is crucial to underpinning mitigation and adaptation strategies.

Following on from previous work documented in M20 for CMIP5 models, we confirmed the importance of the change in SPV strength in driving the extratropical SH circulation response into the future, as manifested through the jet. We additionally quantified the role of SIE decline in influencing the pattern of climate response, which we found to be more influential in summer than winter, in terms of the midlatitude jet response, particularly for the East Antarctic sector. Although the sensitivity of the jet response to SIE decline is found to be about half the magnitude overall relative to the delay in SPV breakdown in summer, we importantly demonstrated that changes in SIE significantly modulate the projected strengthening

and poleward displacement of the jet, according to CMIP6 models, by a factor of 2 or more. This finding is contrary to idealized studies and those more focused on interannual time scales in the literature. For instance, Kidston et al. (2011) found minimal influence of Antarctic sea ice on jet position, particularly during summer, due to the latitudinal offset between the baroclinic zone and the sea ice margin (strongest low-level meridional temperature gradient). As discussed earlier in section 3, the importance of sea ice in determining jet strengthening in CMIP5 has, however, been noted previously (Bracegirdle et al. 2018), but the reasons for this may not be physical and require further investigation. Although we did not explore the role of upper-tropospheric TW directly in this study, as another robust feature of climate change simulated by models, we were able interpret our results with direct reference to earlier findings from M20. The modulation of including TW as an additional third predictor in our storylines was nevertheless tested and found to have a small impact on the storyline differences (see Figs. S13 and S14 for summer and winter respectively). Although U850 was determined to be very sensitive, even more so than the SPV predictor, the impact on explained variance was generally small at high latitudes in particular (Fig. S6).

By evaluating the diagnostic performance of each seasonal MLR model, we found remarkable similarity with M20 for summer in terms of the sensitivity of the jet response to each predictor (up to 70% explained variance near to both the equatorward and poleward flank of the climatological jet location). This is despite having used SIE decline as a predictor in this study instead of upper tropospheric TW. Through investigation of the sensitivity of the jet response to each MLR predictor, we found the influence of SIE decline to be broadly spatially coincident with that of upper tropospheric TW (and of consistent sign). By contrast, the signal provided by the winter MLR model is considerably different to that shown in M20 and found to be substantially weaker than for summer (up to ~35% explained variance). We again, however, confirm that the sensitivity of the jet response to SPV strengthening here strongly resembles that found by M20 and thus, the difference arises due to a contrasting pattern in sensitivity provided by the SIE loss term (in place of upper-tropospheric TW). Thus, the storylines generated here for winter differ more substantially. Given the high-latitude focus of this study, we are nevertheless encouraged by the larger explained variance in circulation response over adjacent seas surrounding Antarctica in winter, using the predictor combination selected here. We furthermore confirm that a strong correlation ($r > 0.6$) exists between the model simulated and MLR predicted values in lower tropospheric jet strengthening (Fig. S15) during summer, as well as Antarctic warming ($r \sim 0.9$) and high-latitude wetting ($r \sim 0.6$–$0.7$) for both seasons (Figs. S16 and S17, respectively), verifying the robustness of each statistical model.

Although our evaluations are all based on a single realization (ensemble member) for each model, we investigated the sensitivity of our results to internal variability for a subset of models with multiple available realizations. We found that the results are highly likely to be insensitive to the choice of realization or using a computed model ensemble mean (see the internal variability assessment of the supplemental material). More influential to the storyline results was the inclusion of model outliers in the climate-mean state of the two predictors during the reference period (1985–2014), particularly for SIE. Models outside $2\sigma$ of the multimodel mean (which is in close agreement with ERA5) were excluded for each season, and also those using the IIEE metric for SIE (ensuring models with realistic overall sea ice coverage but with notably poor spatial representation were omitted). Although assignment of such tolerance thresholds is inherently subjective, the choices made in this study are easily justified as models deemed outliers are far removed from the multimodel mean (see the historical simulation assessment of the supplemental material).

We also evaluated separately model performance in simulating both key surface variables (U850 and T2m) and the selected predictors, using both an RMSE (IIEE for sea ice) and variance metric. This important novel addition in the context of the storyline approach serves to inform the wider community of the relative performance of simulating the historical climate, which may be used to inform decisions of which GCM should be used to help drive regional climate models. An overall performance score was assigned for each model, both for summer and winter, according to whether the models exceeded a set tolerance threshold for the variables and metrics considered. By implementing this straightforward scoring approach, we identified models most representative of each storyline with the ability to accurately simulate the historical climate.

## 6. Conclusions

### a. Summary

We used the storyline approach developed by Zappa and Shepherd (2017) to derive physically plausible scenarios of Antarctic climate change for the end of the century (2070–99), following SSP5-8.5. These scenarios were conditioned upon 1) the magnitude of projected Southern Hemisphere SIE decline and 2) either the degree of wintertime strengthening of the SPV or its delayed summer breakdown. Four storylines were produced for both summer and winter, centered around the multimodel mean response in highlighting the uncertainty in CMIP6 model projections relevant to wider society and global ecosystems. This information is critical for end users such as ecologists and policymakers in determining appropriate future mitigation and adaptation measures (van Vuuren et al. 2011b; Harris et al. 2014; Hughes et al. 2022). Examples include species distribution modeling (e.g., Beaumont et al. 2008) and conservation of marine fisheries (Trathan and Agnew 2010).

Although common features emerge for all storylines, such as the strengthening and poleward shift of the tropospheric jet, the magnitude of this change was found to vary by a factor of 2 or more with important consequences for Antarctic surface warming. This is consistent with our finding that the sensitivity of the lower-tropospheric jet response is approximately twice as large for winter SPV strengthening or delayed summer breakdown relative to SIE decline overall, albeit with large variability between individual sectors for each season. As confirmed from

previous studies, the former acts to strengthen and shift the midlatitude jet poleward, while the latter offsets this tendency as the low-level meridional temperature gradient is typically weakened (Bader et al. 2013; England et al. 2018; Bracegirdle et al. 2018). As evidenced from the derived storylines and associated jet changes, decomposed each in terms of the change in jet strength and position, a strengthening and poleward shift of the jet acts to limit surface warming, except over the Antarctic Peninsula, by reducing meridional transport, with very little sensitivity to the degree of poleward shift in the jet. The largest precipitation response is however associated with a high SIE loss/strong SPV strengthening storyline and we find that the poleward shift of the jet largely determines the magnitude of high-latitude wetting (particularly between ~55° and 70°S) and subtropical drying. The much greater similarity between storylines for precipitation response in each season can be attributed to the strong thermodynamic control of precipitation changes across high-latitude regions (IPCC 2022), meaning that residual differences are important to highlight as the sensitivity to dynamical influence thus emerges.

### b. *Limitations and future research*

This work was motivated primarily by the needs of the regional climate modeling community to select GCMs from CMIP6 for dynamical downscaling, and the need for this data to support impact assessments in the polar regions (e.g., Lee et al. 2022). However, the list of recommended GCMs for downscaling is large considering the computational costs of running multiple RCMs. As such, future work will consider further refinements to the list. For example, a key focus would be to develop a more sophisticated historical performance score that overcomes some of the limitations of the score used here. Such a score should account for model representation of the underlying key processes and mechanisms, through computation of a series of diagnostics (e.g., wave activity fluxes), particularly in connection with climatological features such as the Amundsen Sea low. Such work may help to quantitatively assess the likelihood of potential storyline attributes occurring in the future.

This study focused on the response of the near-surface climate but investigations of different plausible outcomes for the Southern Ocean are of importance, particularly in the context of the social and environmental impacts of climate change (e.g., marine ecosystems). However, this is beyond the scope of the current work but forms the basis of planned future work, both in terms of storyline impacts for ocean features (e.g., the Antarctic Circumpolar Current) and associated changes to marine species (e.g., phytoplankton). Work is also ongoing to establish the degree of linearity (scaling) of the storyline responses for lower-impact pathways (most notably SSP3-7.0). Another priority is to understand the influence of emergent relationships, particularly concerning sea ice, on the results presented here. However, as shown for the Northern Hemisphere, models with the same sea ice forcing may even respond differently (Smith et al. 2022), motivating a detailed investigation worthy of a separate study. We suggest disentanglement of the emergent constraint (historical SIE has a very strong bearing on future SIE loss) across CMIP6 models, invoking use of coordinated model experiments such as from the Polar Amplification Model Intercomparison Project (PAMIP) (Smith et al. 2019). Concerning the sensitivity of the jet to different storyline predictors, a more detailed assessment is required to help understand the extent to which this is related to physical relationships, separate from constraints such as sampling. This may be tested through cross-comparison of results using CMIP5 models with that produced here, to elucidate the sensitivity of our results to model selection.

*Acknowledgments.* This study was undertaken as part of the EU Horizon 2020 PolarRES project (https://polarres.eu/) and was funded under grant agreement number: 101003590. The authors thank the EU commission for facilitating this research. The lead author RSW would additionally like to thank Siv K. Lauvset (NORCE) for her general comments in helping to improve the quality of the manuscript and Tony Phillips (BAS) for technical support pertaining to data acquisition and computing facilities using the Jasmin data analysis facility (https://www.ceda.ac.uk/services/jasmin/). The work of the World Climate Research Programme in coordinating CMIP6 as part of the core Working Group on Coupled Modeling is gratefully acknowledged, in addition to each contributing modeling center in producing and disseminating model output via the Earth System Grid Federation (ESGF). Finally, we thank the editor and three anonymous reviewers for their input in helping us to improve the quality and impact of the study.

*Data availability statement.* CMIP6 model output was accessed using both the baspy Python package (https://github.com/scotthosking/baspy) and the Pangeo integrated software platform (https://pangeo.io/). ERA5 data was retrieved from the Copernicus Climate Change Service (C3S) Climate Data Store.

## REFERENCES

Allison, L. C., H. L. Johnson, D. P. Marshall, and D. R. Munday, 2010: Where do winds drive the Antarctic Circumpolar Current? *Geophys. Res. Lett.*, **37**, L12605, https://doi.org/10.1029/2010GL043355.

Amos, M., and Coauthors, 2020: Projecting ozone hole recovery using an ensemble of chemistry–climate models weighted by model performance and independence. *Atmos. Chem. Phys.*, **20**, 9961–9977, https://doi.org/10.5194/acp-20-9961-2020.

Bader, J., M. Flügge, N. G. Kvamstø, M. D. S. Mesquita, and A. Voigt, 2013: Atmospheric winter response to a projected future Antarctic sea-ice reduction: A dynamical analysis. *Climate Dyn.*, **40**, 2707–2718, https://doi.org/10.1007/s00382-012-1507-9.

Beaumont, L. J., L. Hughes, and A. J. Pitman, 2008: Why is the choice of future climate scenarios for species distribution modelling important? *Ecol. Lett.*, **11**, 1135–1146, https://doi.org/10.1111/j.1461-0248.2008.01231.x.

Bracegirdle, T. J., D. B. Stephenson, J. Turner, and T. Phillips, 2015: The importance of sea ice area biases in 21st century multimodel projections of Antarctic temperature and precipitation.

*Geophys. Res. Lett.*, **42**, 10 832–10 839, https://doi.org/10.1002/2015GL067055.

——, P. Hyder, and C. R. Holmes, 2018: CMIP5 diversity in southern westerly jet projections related to historical sea ice area: Strong link to strengthening and weak link to shift. *J. Climate*, **31**, 195–211, https://doi.org/10.1175/JCLI-D-17-0320.1.

——, G. Krinner, M. Tonelli, F. A. Haumann, K. A. Naughten, T. Rackow, L. A. Roach, and I. Wainer, 2020: Twenty first century changes in Antarctic and Southern Ocean surface climate in CMIP6. *Atmos. Sci. Lett.*, **21**, e984, https://doi.org/10.1002/asl.984.

Campitelli, E., L. B. Díaz, and C. Vera, 2022: Assessment of zonally symmetric and asymmetric components of the southern annular mode using a novel approach. *Climate Dyn.*, **58**, 161–178, https://doi.org/10.1007/s00382-021-05896-5.

Cannon, A. J., 2020: Reductions in daily continental-scale atmospheric circulation biases between generations of global climate models: CMIP5 to CMIP6. *Environ. Res. Lett.*, **15**, 064006, https://doi.org/10.1088/1748-9326/ab7e4f.

Ceppi, P., and T. G. Shepherd, 2019: The role of the stratospheric polar vortex for the austral jet response to greenhouse gas forcing. *Geophys. Res. Lett.*, **46**, 6972–6979, https://doi.org/10.1029/2019GL082883.

Chemke, R., Y. Ming, and J. Yuval, 2022: The intensification of winter mid-latitude storm tracks in the Southern Hemisphere. *Nat. Climate Change*, **12**, 553–557, https://doi.org/10.1038/s41558-022-01368-8.

Chen, G., Zhang, P., and Lu, J., 2020: Sensitivity of the latitude of the westerly jet stream to climate forcing. *Geophys. Res. Lett.*, **47**, e2019GL086563, https://doi.org/10.1029/2019GL086563.

Chen, W., D. Jiang, X. Lang, and Z. Tian, 2022: Improved skill of Coupled Model Intercomparison Project phase 6 over phase 5 models in reproducing weather regimes in East Asia. *Int. J. Climatol.*, **42**, 9271–9287, https://doi.org/10.1002/joc.7817.

Collins, M., R. E. Chandler, P. M. Cox, J. M. Huthnance, J. Rougier, and D. B. Stephenson, 2012: Quantifying future climate change. *Nat. Climate Change*, **2**, 403–409, https://doi.org/10.1038/nclimate1414.

Cos, J., F. Doblas-Reyes, M. Jury, R. Marcos, P.-A. Bretonnière, and M. Samsó, 2022: The Mediterranean climate change hotspot in the CMIP5 and CMIP6 projections. *Earth Syst. Dyn.*, **13**, 321–340, https://doi.org/10.5194/esd-13-321-2022.

Deng, K., C. Azorin-Molina, S. Yang, C. Hu, G. Zhang, L. Minola, and D. Chen, 2022: Changes of Southern Hemisphere westerlies in the future warming climate. *Atmos. Res.*, **270**, 106040, https://doi.org/10.1016/j.atmosres.2022.106040.

Deser, C., A. Phillips, V. Bourdette, and H. Teng, 2012: Uncertainty in climate change projections: The role of internal variability. *Climate Dyn.*, **38**, 527–546, https://doi.org/10.1007/s00382-010-0977-x.

Dhomse, S. S., and Coauthors, 2018: Estimates of ozone return dates from chemistry-climate model initiative simulations. *Atmos. Chem. Phys.*, **18**, 8409–8438, https://doi.org/10.5194/acp-18-8409-2018.

Doddridge, E. W., and J. Marshall, 2017: Modulation of the seasonal cycle of Antarctic sea ice extent related to the southern annular mode. *Geophys. Res. Lett.*, **44**, 9761–9768, https://doi.org/10.1002/2017GL074319.

——, ——, H. Song, J.-M. Campin, M. Kelley, and L. Nazarenko, 2019: Eddy compensation dampens Southern Ocean sea surface temperature response to westerly wind trends. *Geophys. Res. Lett.*, **46**, 4365–4377, https://doi.org/10.1029/2019GL082758.

Dorrington, J., K. Strommen, and F. Fabiano, 2022: Quantifying climate model representation of the wintertime Euro-Atlantic circulation using geopotential-jet regimes. *Wea. Climate Dyn.*, **3**, 505–533, https://doi.org/10.5194/wcd-3-505-2022.

England, M., L. Polvani, and L. Sun, 2018: Contrasting the Antarctic and Arctic atmospheric responses to projected sea ice loss in the late twenty-first century. *J. Climate*, **31**, 6353–6370, https://doi.org/10.1175/JCLI-D-17-0666.1.

Eyring, V., and Coauthors, 2013: Long-term ozone changes and associated climate impacts in CMIP5 simulations. *J. Geophys. Res. Atmos.*, **118**, 5029–5060, https://doi.org/10.1002/jgrd.50316.

——, S. Bony, G. A. Meehl, C. A. Senior, B. Stevens, R. J. Stouffer, and K. E. Taylor, 2016: Overview of the Coupled Model Intercomparison Project Phase 6 (CMIP6) experimental design and organization. *Geosci. Model Dev.*, **9**, 1937–1958, https://doi.org/10.5194/gmd-9-1937-2016.

Flato, G. M., 2004: Sea-ice and its response to $CO_2$ forcing as simulated by global climate models. *Climate Dyn.*, **23**, 229–241, https://doi.org/10.1007/s00382-004-0436-7.

Gille, S. T., 2008: Decadal-scale temperature trends in the Southern Hemisphere Ocean. *J. Climate*, **21**, 4749–4765, https://doi.org/10.1175/2008JCLI2131.1.

Goessling, H. F., S. Tietsche, J. J. Day, E. Hawkins, and T. Jung, 2016: Predictability of the Arctic sea ice edge. *Geophys. Res. Lett.*, **43**, 1642–1650, https://doi.org/10.1002/2015GL067232.

Goosse, H., and Coauthors, 2018: Quantifying climate feedbacks in polar regions. *Nat. Commun.*, **9**, 1919, https://doi.org/10.1038/s41467-018-04173-0.

Goyal, R., M. Jucker, A. Sen Gupta, H. H. Hendon, and M. H. England, 2021: Zonal wave 3 pattern in the Southern Hemisphere generated by tropical convection. *Nat. Geosci.*, **14**, 732–738, https://doi.org/10.1038/s41561-021-00811-3.

Harris, R. M. B., M. R. Grose, G. Lee, N. L. Bindoff, L. L. Porfirio, and P. Fox-Hughes, 2014: Climate projections for ecologists. *Wiley Interdiscip. Rev.: Climate Change*, **5**, 621–637, https://doi.org/10.1002/wcc.291.

Hauck, J., C. Völker, T. Wang, M. Hoppema, M. Losch, and D. A. Wolf-Gladrow, 2013: Seasonally different carbon flux changes in the Southern Ocean in response to the southern annular mode. *Global Biogeochem. Cycles*, **27**, 1236–1245, https://doi.org/10.1002/2013GB004600.

Hersbach, H., and Coauthors, 2020: The ERA5 global reanalysis. *Quart. J. Roy. Meteor. Soc.*, **146**, 1999–2049, https://doi.org/10.1002/qj.3803.

Hughes, K. A., R. D. Cavanagh, and P. Convey, 2022: Advancing Antarctic climate change policy: Upcoming opportunities for scientists and policymakers to work together. *Antarct. Sci.*, **34**, 403–407, https://doi.org/10.1017/S095410202200044X.

IPCC, 2022: *Climate Change 2022: Impacts, Adaptation, and Vulnerability*. Cambridge University Press, 3056 pp., https://doi.org/10.1017/9781009325844.

John, A., H. Douville, A. Ribes, and P. Yiou, 2022: Quantifying CMIP6 model uncertainties in extreme precipitation projections. *Wea. Climate Extremes*, **36**, 100435, https://doi.org/10.1016/j.wace.2022.100435.

Karpechko, A. Y., and Coauthors, 2022: Northern Hemisphere stratosphere-troposphere circulation change in CMIP6 models: 1. Inter-model spread and scenario sensitivity. *J. Geophys. Res. Atmos.*, **127**, e2022JD036992, https://doi.org/10.1029/2022JD036992.

Kidston, J., A. S. Taschetto, D. W. J. Thompson, and M. H. England, 2011: The influence of Southern Hemisphere sea-ice extent on the latitude of the mid-latitude jet stream.

*Geophys. Res. Lett.*, **38**, L15804, https://doi.org/10.1029/2011GL048056.

Kohyama, T., and D. L. Hartmann, 2016: Antarctic sea ice response to weather and climate modes of variability. *J. Climate*, **29**, 721–741, https://doi.org/10.1175/JCLI-D-15-0301.1.

Landschützer, P., N. Gruber, and D. C. E. Bakker, 2016: Decadal variations and trends of the global ocean carbon sink. *Global Biogeochem. Cycles*, **30**, 1396–1417, https://doi.org/10.1002/2015GB005359.

Lee, H., N. Johnston, L. Nieradzik, A. Orr, R. H. Mottram, W. J. van de Berg, and P. A. Mooney, 2022: Toward effective collaborations between regional climate modeling and impacts-relevant modeling studies in polar regions. *Bull. Amer. Meteor. Soc.*, **103**, E1866–E1874, https://doi.org/10.1175/BAMS-D-22-0102.1.

Lenton, A., and R. J. Matear, 2007: Role of the Southern Annular Mode (SAM) in southern ocean $CO_2$ uptake. *Global Biogeochem. Cycles*, **21**, GB2016, https://doi.org/10.1029/2006GB002714.

Li, C., J.-S. von Storch, and J. Marotzke, 2013: Deep-ocean heat uptake and equilibrium climate response. *Climate Dyn.*, **40**, 1071–1086, https://doi.org/10.1007/s00382-012-1350-z.

Limpasuvan, V., and D. L. Hartmann, 1999: Eddies and the annular modes of climate variability. *Geophys. Res. Lett.*, **26**, 3133–3136, https://doi.org/10.1029/1999GL010478.

Marshall, G. J., R. L. Fogt, J. Turner, and K. R. Clem, 2022: Can current reanalyses accurately portray changes in Southern Annular Mode structure prior to 1979? *Climate Dyn.*, **59**, 3717–3740, https://doi.org/10.1007/s00382-022-06292-3.

Meredith, M. P., and A. M. Hogg, 2006: Circumpolar response of Southern Ocean eddy activity to a change in the southern annular mode. *Geophys. Res. Lett.*, **33**, L16608, https://doi.org/10.1029/2006GL026499.

Mindlin, J., T. G. Shepherd, C. S. Vera, M. Osman, G. Zappa, R. W. Lee, and K. I. Hodges, 2020: Storyline description of Southern Hemisphere midlatitude circulation and precipitation response to greenhouse gas forcing. *Climate Dyn.*, **54**, 4399–4421, https://doi.org/10.1007/s00382-020-05234-1.

——, Shepherd, T. G., Vera, C., and Osman, M., 2021: Combined effects of global warming and ozone depletion/recovery on Southern Hemisphere atmospheric circulation and regional precipitation. *Geophys. Res. Lett.*, **48**, e2021GL092568, https://doi.org/10.1029/2021GL092568.

O'Neill, B. C., and Coauthors, 2016: The Scenario Model Intercomparison Project (ScenarioMIP) for CMIP6. *Geosci. Model Dev.*, **9**, 3461–3482, https://doi.org/10.5194/gmd-9-3461-2016.

Orr, A., T. J. Bracegirdle, J. S. Hosking, T. Jung, J. D. Haigh, T. Phillips, and W. Feng, 2012: Possible dynamical mechanisms for Southern Hemisphere climate change due to the ozone hole. *J. Atmos. Sci.*, **69**, 2917–2932, https://doi.org/10.1175/JAS-D-11-0210.1.

Palmer, T. N., F. J. Doblas-Reyes, R. Hagedorn, and A. Weisheimer, 2005: Probabilistic prediction of climate using multi-model ensembles: From basics to applications. *Philos. Trans. Roy. Soc.*, **B360**, 1991–1998, https://doi.org/10.1098/rstb.2005.1750.

Pithan, F., and T. Mauritsen, 2014: Arctic amplification dominated by temperature feedbacks in contemporary climate models. *Nat. Geosci.*, **7**, 181–184, https://doi.org/10.1038/ngeo2071.

Polvani, L. M., D. W. Waugh, G. J. Correa, and S.-W. Son, 2011: Stratospheric ozone depletion: The main driver of twentieth-century atmospheric circulation changes in the Southern Hemisphere. *J. Climate*, **24**, 795–812, https://doi.org/10.1175/2010JCLI3772.1.

Purich, A., W. Cai, M. H. England, and T. Cowan, 2016: Evidence for link between modelled trends in Antarctic sea ice and underestimated westerly wind changes. *Nat. Commun.*, **7**, 10409, https://doi.org/10.1038/ncomms10409.

Raphael, M. N., 2003: Impact of observed sea-ice concentration on the Southern Hemisphere extratropical atmospheric circulation in summer. *J. Geophys. Res.*, **108**, 4687, https://doi.org/10.1029/2002JD003308.

Revell, L. E., Robertson, F., Douglas, H., Morgenstern, O. and Frame, D., 2022: Influence of ozone forcing on 21st century Southern Hemisphere surface westerlies in CMIP6 models. *Geophys. Res. Lett.*, **49**, e2022GL098252, https://doi.org/10.1029/2022GL098252.

Roach, L. A., and Coauthors, 2020: Antarctic sea ice area in CMIP6. *Geophys. Res. Lett.*, **47**, e2019GL086729, https://doi.org/10.1029/2019GL086729.

Rogers, J. C., and H. van Loon, 1982: Spatial variability of sea level pressure and 500 mb height anomalies over the Southern Hemisphere. *Mon. Wea. Rev.*, **110**, 1375–1392, https://doi.org/10.1175/1520-0493(1982)110<1375:SVOSLP>2.0.CO;2.

Sallée, J. B., K. G. Speer, and S. R. Rintoul, 2010: Zonally asymmetric response of the Southern Ocean mixed-layer depth to the Southern Annular Mode. *Nat. Geosci.*, **3**, 273–279, https://doi.org/10.1038/ngeo812.

Schneider, D. P., C. Deser, and T. Fan, 2015: Comparing the impacts of tropical SST variability and Polar stratospheric ozone loss on the Southern Ocean westerly winds. *J. Climate*, **28**, 9350–9372, https://doi.org/10.1175/JCLI-D-15-0090.1.

Schneider, T., P. A. O'Gorman, and X. J. Levine, 2010: Water vapor and the dynamics of climate changes. *Rev. Geophys.*, **48**, RG3001, https://doi.org/10.1029/2009RG000302.

Screen, J. A., N. P. Gillett, A. Y. Karpechko, and D. P. Stevens, 2010: Mixed layer temperature response to the Southern Annular Mode: Mechanisms and model representation. *J. Climate*, **23**, 664–678, https://doi.org/10.1175/2009JCLI2976.1.

——, Bracegirdle, T. J., and Simmonds, I., 2018: Polar climate change as manifest in atmospheric circulation. *Curr. Climate Change Rep.*, **4**, 383–395, https://doi.org/10.1007/s40641-018-0111-4.

Shepherd, T. G., 2014: Atmospheric circulation as a source of uncertainty in climate change projections. *Nat. Geosci.*, **7**, 703–708, https://doi.org/10.1038/ngeo2253.

Simmonds, I., K. Keay, and E.-P. Lim, 2003: Synoptic activity in the seas around Antarctica. *Mon. Wea. Rev.*, **131**, 272–288, https://doi.org/10.1175/1520-0493(2003)131<0272:SAITSA>2.0.CO;2.

Simpkins, G. R., L. M. Ciasto, D. W. J. Thompson, and M. H. England, 2012: Seasonal relationships between large-scale climate variability and Antarctic sea ice concentration. *J. Climate*, **25**, 5451–5469, https://doi.org/10.1175/JCLI-D-11-00367.1.

Smith, D. M., and Coauthors, 2019: The Polar Amplification Model Intercomparison Project (PAMIP) contribution to CMIP6: Investigating the causes and consequences of polar amplification. *Geosci. Model Dev.*, **12**, 1139–1164, https://doi.org/10.5194/gmd-12-1139-2019.

——, and Coauthors, 2022: Robust but weak winter atmospheric circulation response to future Arctic sea ice loss. *Nat. Commun.*, **13**, 727, https://doi.org/10.1038/s41467-022-28283-y.

Son, S.-W., and Coauthors, 2008: The impact of stratospheric ozone recovery on the Southern Hemisphere westerly jet. *Science*, **320**, 1486–1489, https://doi.org/10.1126/science.1155939.

——, N. F. Tandon, L. M. Polvani, and D. W. Waugh, 2009: Ozone hole and Southern Hemisphere climate change. *Geophys. Res. Lett.*, **36**, L15705, https://doi.org/10.1029/2009GL038671.

Spence, P., S. M. Griffies, M. H. England, A. M. Hogg, O. A. Saenko, and N. C. Jourdain, 2014: Rapid subsurface warming and circulation changes of Antarctic coastal waters by poleward shifting winds. *Geophys. Res. Lett.*, **41**, 4601–4610, https://doi.org/10.1002/2014GL060613.

Stouffer, R. J., 2004: Time scales of climate response. *J. Climate*, **17**, 209–217, https://doi.org/10.1175/1520-0442(2004)017<0209:TSOCR>2.0.CO;2.

Sun, L., G. Chen, and W. A. Robinson, 2014: The role of stratospheric polar vortex breakdown in Southern Hemisphere climate trends. *J. Atmos. Sci.*, **71**, 2335–2353, https://doi.org/10.1175/JAS-D-13-0290.1.

Swart, N. C., J. C. Fyfe, N. Gillett, and G. J. Marshall, 2015: Comparing trends in the southern annular mode and surface westerly jet. *J. Climate*, **28**, 8840–8859, https://doi.org/10.1175/JCLI-D-15-0334.1.

Tebaldi, C., and R. Knutti, 2007: The use of the multi-model ensemble in probabilistic climate projections. *Philos. Trans. Roy. Soc.*, **A365**, 2053–2075, https://doi.org/10.1098/rsta.2007.2076.

Thompson, D. W. J., and J. M. Wallace, 2000: Annular modes in the extratropical circulation. Part I: Month-to-month variability. *J. Climate*, **13**, 1000–1016, https://doi.org/10.1175/1520-0442(2000)013<1000:AMITEC>2.0.CO;2.

——, and S. Solomon, 2002: Interpretation of recent Southern Hemisphere climate change. *Science*, **296**, 895–899, https://doi.org/10.1126/science.1069270.

——, ——, P. J. Kushner, M. H. England, K. M. Grise, and D. J. Karoly, 2011: Signatures of the Antarctic ozone hole in Southern Hemisphere surface climate change. *Nat. Geosci.*, **4**, 741–749, https://doi.org/10.1038/ngeo1296.

Trathan, P. N., and D. Agnew, 2010: Climate change and the Antarctic marine ecosystem: An essay on management implications. *Antarct. Sci.*, **22**, 387–398, https://doi.org/10.1017/S0954102010000222.

van Vuuren, D. P., and Coauthors, 2011a: The representative concentration pathways: An overview. *Climatic Change*, **109**, 5, https://doi.org/10.1007/s10584-011-0148-z.

——, and Coauthors, 2011b: The use of scenarios as the basis for combined assessment of climate change mitigation and adaptation. *Global Environ. Change*, **21**, 575–591, https://doi.org/10.1016/j.gloenvcha.2010.11.003.

Waugh, D. W., L. Oman, P. A. Newman, R. S. Stolarski, S. Pawson, J. E. Nielsen, and J. Perlwitz, 2009: Effect of zonal asymmetries in stratospheric ozone on simulated Southern Hemisphere climate trends. *Geophys. Res. Lett.*, **36**, L18701, https://doi.org/10.1029/2009GL040419.

——, A. Banerjee, J. C. Fyfe, and L. M. Polvani, 2020: Contrasting recent trends in Southern Hemisphere westerlies across different ocean basin. *Geophys. Res. Lett.*, **47**, e2020GL088890, https://doi.org/10.1029/2020GL088890.

Williams, L. N., S. Lee, and S.-W. Son, 2007: Dynamics of the Southern Hemisphere spiral jet. *J. Atmos. Sci.*, **64**, 548–563, https://doi.org/10.1175/JAS3939.1.

World Meteorological Organization (WMO), 2022: Executive summary. Scientific Assessment of Ozone Depletion: 2022. GAW Rep. 278, 56 pp., https://csl.noaa.gov/assessments/ozone/2022/.

Xie, S.-P., C. Deser, G. A. Vecchi, J. Ma, H. Teng, and A. T. Wittenberg, 2010: Global warming pattern formation: Sea surface temperature and rainfall. *J. Climate*, **23**, 966–986, https://doi.org/10.1175/2009JCLI3329.1.

Yang, D., J. M. Arblaster, G. A. Meehl, M. H. England, E.-P. Lim, S. Bates, and N. Rosenbloom, 2020: Role of tropical variability in driving decadal shifts in the Southern Hemisphere summertime eddy-driven jet. *J. Climate*, **33**, 5445–5463, https://doi.org/10.1175/JCLI-D-19-0604.1.

Yin, J., J. T. Overpeck, S. M. Griffies, A. Hu, J. L. Russell, and R. J. Stouffer, 2011: Different magnitudes of projected subsurface ocean warming around Greenland and Antarctica. *Nat. Geosci.*, **4**, 524–528, https://doi.org/10.1038/ngeo1189.

Yin, J. H., 2005: A consistent poleward shift of the storm tracks in simulations of 21st century climate. *Geophys. Res. Lett.*, **32**, L18701, https://doi.org/10.1029/2005GL023684.

Zappa, G., and T. G. Shepherd, 2017: Storylines of atmospheric circulation change for European regional climate impact assessment. *J. Climate*, **30**, 6561–6577, https://doi.org/10.1175/JCLI-D-16-0807.1.